aerospace

MDPI

Article

Retrofitted Hydrogen-Electric Propulsion Aircraft: Performance Simulation of Critical Operating Conditions

Wim Lammen *, Pieter-Jan Dewitte and Elise Scheers

Collaborative Engineering Systems Department, Aerospace Vehicles Division, Royal Netherlands Aerospace Centre NLR, Anthony Fokkerweg 2, 1059 Amsterdam, The Netherlands; pieter-jan.dewitte@nlr.nl (P.-J.D.); elise.scheers@nlr.nl (E.S.)

* Correspondence: wim.lammen@nlr.nl; Tel.: +31-88-511-3049

Abstract: Retrofitting regional turboprop aircraft with hydrogen (H_2)-electric powertrains, using fuel cell systems (FCSs), has gained interest in the last decade. This type of powertrain eliminates CO_2, NOx, and fine particle emissions during flight, as FCSs only emit water. In this context, the "Hydrogen Aircraft Powertrain and Storage Systems" (HAPSS) project targets the development of a H_2-electric propulsion system for retrofitting Dash 8-300 series aircraft. The purpose of the study described in this paper is to analyze the performance of the retrofitted H_2-electric aircraft during critical operating conditions. Takeoff, as well as climb, cruise and go-around performances are addressed. The NLR in-house tool MASS (Mission, Aircraft and Systems Simulation) was used for the performance analyses. The results show that the retrofitted H_2-electric aircraft has a slightly increased takeoff distance compared to the Dash 8-300 and it requires a maximum rated shaft power of 1.9 MW per propeller. A total rated FCS output power of 3.1 MW is sufficient to satisfy the takeoff requirements, at the cost of lower cruise altitude and reduced cruise speed as compared to the Dash 8-300. Furthermore, a higher-rated FCS is required to achieve the climb performance required for the typical climb profile of the Dash 8-300.

Keywords: hydrogen-powered aircraft; hydrogen-electric propulsion; retrofitted aircraft; fuel cell systems; performance analysis; mission simulation; powertrains

Academic Editors: Giacomo Silvagni and Vittorio Ravaglioli

Received: 29 November 2024
Revised: 20 January 2025
Accepted: 22 January 2025
Published: 27 January 2025

Citation: Lammen, W.; Dewitte, P.-J.; Scheers, E. Retrofitted Hydrogen-Electric Propulsion Aircraft: Performance Simulation of Critical Operating Conditions. *Aerospace* **2025**, *12*, 95. https://doi.org/10.3390/aerospace12020095

1. Introduction

Reducing greenhouse gas emissions and energy consumption is one of the main challenges for the development of future commercial aircraft. Design efforts to create aircraft with lower energy consumption—e.g., by weight reduction, improved aerodynamic efficiency and more efficient engines—are common in commercial aircraft development. The lower energy consumption also contributes to a reduction in the emissions. However, if kerosene is used as fuel, CO_2 and other greenhouse gasses are still emitted during flight.

In the last decade, alternative fuels and propulsion systems have also gained more attention in order to further reduce the environmental impact of aviation. For instance, battery or hybrid electric powertrains, hydrogen (H_2)-powered propulsion or the use of sustainable aviation fuels (SAF) are being considered. The development of H_2-powered aircraft has recently become a topic of major interest as it presents the opportunity to eliminate CO_2 emissions. H_2 for propulsion cannot be used in current transport aircraft, e.g., because of the absence of adequate H_2 storage systems. Disruptive technologies to enable H_2-powered aircraft are investigated in the European research programs Clean Aviation [1] and Clean Hydrogen [2]. In particular, the onboard use of liquid hydrogen

(LH_2) is under investigation, taking advantage of its more compact storage potential in comparison to compressed gaseous hydrogen (GH_2).

Novel aircraft propulsion concepts are being studied (and developed) either with H_2 combustion engines, H_2 fuel cells delivering electric power for electrically driven propulsors, or a combination of both [3–10]. In 2020, a feasibility study was performed [3] highlighting the potential of H_2 in aviation and recommending further research in this direction. Various aircraft sizes were conceptually assessed, ranging from small regional aircraft with fuel cell-based propulsion to large aircraft with H_2 combustion. Several (more detailed) studies followed, addressing various aircraft sizes. Besides the aforementioned European research programs, aircraft concepts with H_2-powered propulsion are being investigated by Airbus [4] and in several national research initiatives [5–8].

This paper addresses aircraft propulsion by means of fuel cells in combination with electrically driven propellers: H_2-electric propulsion. This type of propulsion provides opportunities to eliminate CO_2, NO_X and fine-particle emissions, as fuel cells only emit water. It also facilitates distributed propulsion layouts (e.g., [4,6,7]) which may have several advantages, such as improved aerodynamic and propulsive efficiency, system redundancy and steering by thrust vectoring [9]. In the aviation sector, H_2-electric propulsion is a technology under development, and it poses several design challenges [10]. For example, difficulties arise for the H_2 storage and distribution on board the aircraft due to the unique properties of the fluid and the stringent requirements in terms of safety, weight and volume. The added weight, volume and packaging of the LH_2 tanks result in weight and drag penalties to the aircraft design. Furthermore, fuel cells need special systems for conditioned air and H_2 supply, and they need an extensive cooling system. These additional systems also result in weight, volume, drag and power penalties which impact the aircraft design.

H_2-electric propulsion is mostly investigated in the context of regional turboprop aircraft (e.g., below 2000 km range) [3–7]. In comparison to the relatively small gas turbines that are employed in regional turboprop aircraft, H_2-electric propulsion systems (HPSs) can result in a higher overall efficiency of the powertrain [3,11]. In this paper, HPS means the combination of fuel cell system, electric distribution, power electronics and electric motors. Although regional aircraft are only a small fraction of global aviation and this will therefore have a limited climate impact, the development and maturation of the H_2 technology for these aircraft may serve as a stepping stone for application in larger aircraft [11].

H_2-electric propulsion can either be applied to new aircraft concepts based on clean sheet design [4], or retrofitted to existing aircraft [12,13]. In the case of clean sheet design aircraft, it is expected that these designs result in optimal performances, taking advantage of the benefits of a larger design space. Retrofitted aircraft have a smaller design space—being restricted by the limitations of the reference aircraft—which may therefore result in suboptimal performance. However, it is foreseen that there will be less certification effort, resulting in a shorter time to market [13]. Several start-ups and established aircraft manufacturers have announced plans to develop H_2-electric aircraft, or have even demonstrated retrofits of existing aircraft [10,14].

In the Netherlands, the "Luchtvaart in Transitie" (Aviation in Transition) program [8] has been established as a pioneering initiative to accelerate sustainability in aviation. Participating partners from the Dutch aviation sector are focused on developing innovative solutions, including energy-efficient technologies, lightweight materials and systems, and carbon-neutral propulsion systems, such as H_2 powertrains. In this framework, the "Hydrogen Aircraft Powertrain and Storage Systems" (HAPSS) project, launched in October 2022 [13,15], concerns the development of commercially viable HAPSS. The objective is to bring this technology to market by the end of the decade, starting from retrofitting of existing regional aircraft. The HAPSS comprise the powertrain from an LH_2 tank to a

Fuel Cell System (FCS), electric motor and propeller, with all required auxiliary systems: thermal management, controls and electric distribution. Figure 1 illustrates the aircraft concept proposed in the HAPSS project. The first case study is the De Havilland Canada Dash 8-300 series aircraft. This regional turboprop aircraft has a 50-passengers capacity. The proposed retrofit approach involves making a limited change to an aircraft that has already been certified.

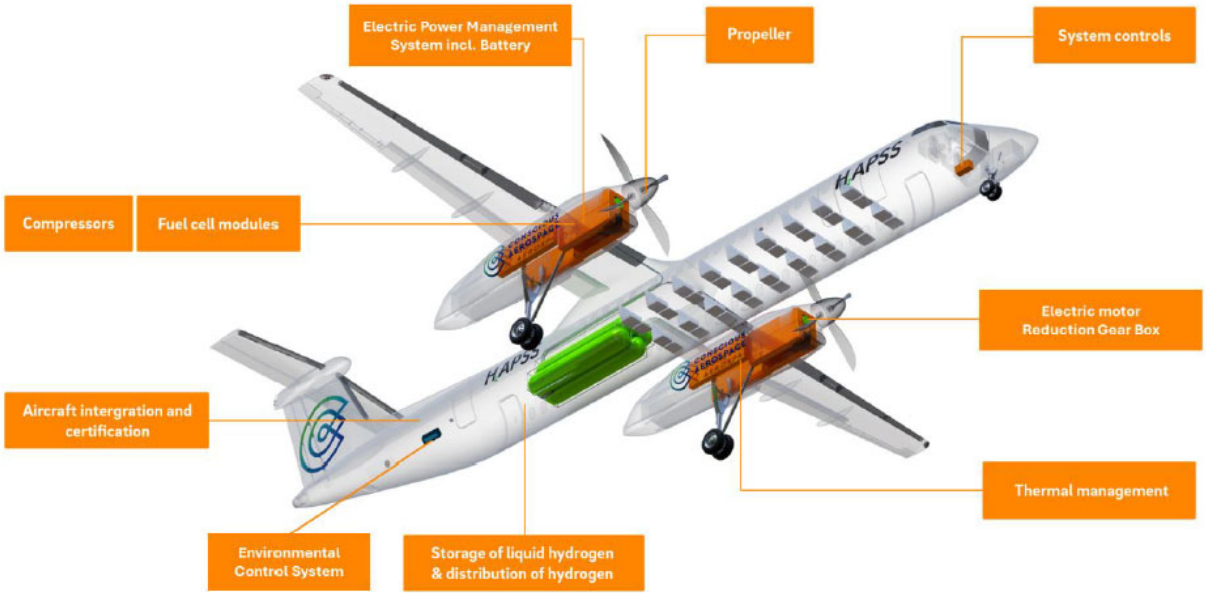

Figure 1. Illustration of the HAPSS aircraft concept, picture adapted from Ref. [13].

Knowledge about the performance and sizing of HPSs, i.e., what operating conditions constrain the design, is still under development [10]. For example, it is yet unclear which design point (takeoff, top of climb, etc.) is critical for the sizing of the HPS and the thermal management system (TMS) for a regional airplane like the Dash 8-300. The objective of the work described in this paper is to understand the performance of the HAPSS aircraft concept during critical mission conditions, i.e., the mission conditions which impact the sizing of the HPS and the TMS, and to compare the performance with the reference kerosene aircraft (the Dash 8-300).

Full mission simulations with the HAPSS aircraft—e.g., for payload and range performance analysis—as well as sizing and performance analysis of the LH_2 storage and distribution system are not in the scope of this paper. Such simulations have been performed already and can be found in Ref. [13]. Instead, this paper focuses on specific mission phases and operating conditions that can be critical for the sizing of the HPS and the TMS. Results from Ref. [13] were re-used in the study, e.g., in terms of the mass breakdown of the retrofitted aircraft.

This paper addresses following research questions:

- What power rating of the HPS is needed to fulfill the takeoff requirements, according to CS-25 [16], and what is the corresponding takeoff distance?
- What is the impact on the TMS, in terms of cooling demand during takeoff?
- What power rating of the HPS is needed to fulfill the go-around (missed approach) requirements, according to CS-25 [16]?
- What are the climb and cruise performances of the HAPSS aircraft for various HPS ratings and operating conditions?

The remainder of this paper is structured as follows. Section 2 describes the applied methods and developed models to simulate the performance of the reference aircraft

and the HAPSS aircraft for various mission conditions. In Section 3, the performance simulation results are presented for the various mission phases and operating conditions. In Section 4, the simulation results are discussed, in relation to the model assumptions. Items for further research are identified. Section 5 provides a summary of the findings and concluding remarks.

2. Materials and Methods

This section contains the description of the applied methods, models, parameter settings and assumptions to carry out the mission performance simulations. First, the aircraft-level assumptions are described (applied reference aircraft data and assumptions for the retrofitted H_2-electric aircraft). Second, the tooling is described, including the underlying performance models. These include the mission models, aircraft equations of motion, aerodynamic models, propeller model, engine model (for the reference aircraft) and HPS model (including the FCS and electric components, for the H_2-electric aircraft). Models of the LH_2 fuel system are not in the scope of this paper (as explained in the previous section). Fixed aircraft mass assumptions are applied, based on Ref. [13].

2.1. Aircraft-Level Assumptions

In our study, the 311 model of the Dash 8-300 aircraft was selected as the reference aircraft, because, for this model, public performance data could be retrieved [17], and because this model was used in Ref. [13] as well. Key parameters of the reference aircraft which are used in this study are summarized in Table 1, while an illustration of the aircraft is provided in Figure 2. These parameters serve as a baseline for the performance simulations of both the reference and the retrofitted aircraft.

Table 1. Applied reference aircraft and HAPSS aircraft parameters.

Parameters	Reference Aircraft Values [17–20]	HAPSS Aircraft Values [13]
Aircraft model	311	311
Range	920 NM (1704 km)	750 km
Maximum cruise altitude	25,000 ft (7620 m)	25,000 ft (7620 m)
Cruise true air speed	133 m/s (480 km/h)	133 m/s (480 km/h)
Maximum takeoff mass (MTOM)	19,505 kg	19,051 kg
Maximum landing mass (MLM)	19,051 kg	19,051 kg
Design payload mass	5300 kg	3089 kg
Operational empty mass (OEM)	11,653 kg	15,622 kg
Wing area (S_w)	56.3 m^2	56.3 m^2
Wing span (B_w)	27.4 m	27.4 m
Number of engines/propellers (N_p)	2	2
Engine type	Pratt & Whitney PW123	HPS (see Section 2.7)
Maximum takeoff (shaft) power, per engine	1775 kW	1775 kW
Propeller type	Hamilton Sundstrand 14SF	Hamilton Sundstrand 14SF
Propeller diameter (D_p)	3.96 m	3.96 m
Number of propeller blades (B_p)	4	4

Figure 2. Air New Zealand Dash 8-300 (2017), copyright picture by Jordan Tan, via Shutterstock (StockFoto ID: 729358585).

Some of the mass parameters in Table 1 are adapted for the retrofitted H_2-electric aircraft (also referred to as the HAPSS aircraft). The sizing of the HAPSS aircraft is described in Ref. [13]. From this sizing process, the resulting aircraft mass breakdown is adopted:

- The aircraft operational empty mass (OEM) was increased from 11.6 t to 15.6 t for the HAPSS aircraft. This increase is due to the additional HPS and LH_2 fuel system masses (including tanks) [13].
- The maximum takeoff mass (MTOM) is lowered to the maximum landing mass of the reference aircraft (19.1 t). The reason for this decrease is that it is foreseen that the HAPSS aircraft cannot dump any fuel after takeoff, in case of emergency [13].
- Due to the increased OEM and decreased MTOM, the payload mass is decreased to 3.1 t, and the range is lowered to 750 km [13].

The maximum cruise altitude, the cruise true air speed (TAS) and maximum takeoff shaft power are (initially) inherited from the reference aircraft. However, they will be assessed by means of the performance simulations with the HAPSS aircraft (see Section 3.2).

2.2. Mission Models

2.2.1. Mission Performance Tooling

The aircraft modelling and corresponding performance analysis was carried out using the NLR in-house tool MASS (Mission, Aircraft and Systems Simulation for energy performance analysis [21]). MASS is a MATLAB-based tool (R2024b) for mission performance and sizing analysis of aircraft and powertrains. Various aircraft powertrain configurations can be simulated, e.g., conventional turboprop, (hybrid) electric or H_2-electric. System models of various complexity levels can be applied. The system models used in this paper are described in the following sections. With MASS, usually the fuel flow and total power are calculated as function of mission time in order to predict total trip fuel, energy consumption and emissions [11]. This is illustrated by the black arrows in Figure 3. The mission variables are expressed as function of time, by means of interpolation between specified speed, altitude and rate of climb (ROC) combinations, which can be retrieved from public sources such as [22,23]. Figure 4 depicts a standard mission profile of the conventional Dash 8-300 aircraft.

For specific use cases—when power values are known and when more detailed (acceleration, speed and ROC) performances must be determined, during specified mission segments (e.g., takeoff, climb or go-around)—an alternative simulation method was implemented in MASS, illustrated by the orange arrows in Figure 3.

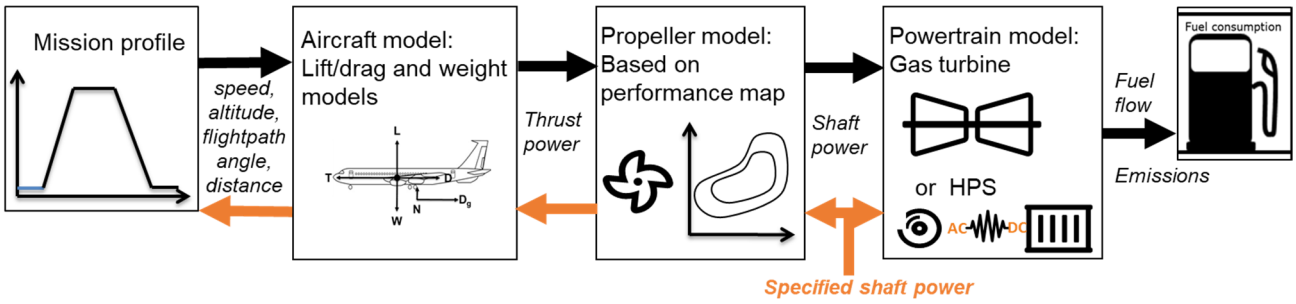

Figure 3. Performance simulation model scheme.

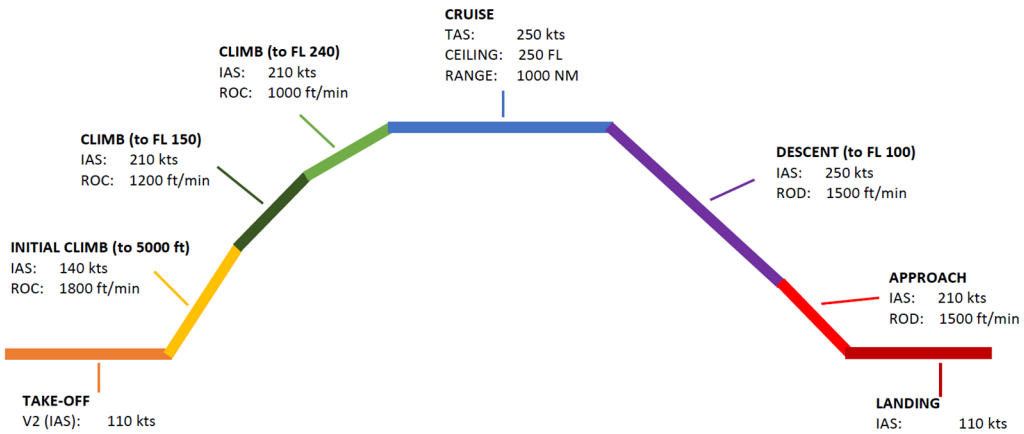

Figure 4. Example mission profile information for the Dash 8-300, adapted from Ref. [22].

2.2.2. Modelling of the Takeoff Phase

The takeoff phase of an aircraft can be subdivided into several segments determined by flap, landing gear and power settings [16]. The segments are bounded by specific speed and altitude values. The subdivision of the takeoff phase is illustrated in Figure 5. Two scenarios are considered: all-engines-operative (AEO) and the one-engine-inoperative (OEI). The speeds that mark the segment bounds are:

- Initial speed v_0. This is the start speed of the takeoff run, typically 0 m/s.
- Decision speed v_1. In case an engine failure takes place below this speed, the aircraft must be able to brake and come to a standstill before the end of the runway. When the aircraft has reached v_1, it must be able to continue the takeoff with the other engine(s) that is/are still in operation.
- Rotation speed v_R. At this speed the aircraft starts it rotation, by using the control surfaces.
- Liftoff speed v_{LOFF}. At this speed the aircraft lifts off and its altitude increases with respect to the ground level.
- Obstacle clearance speed v_2. The aircraft must have reached this speed when reaching 35 ft (10.7 m) altitude above the ground.
- Climb speed $v_{enroute}$. This is the indicated air speed for (the first part of) the climb phase.

International Standard Atmosphere (ISA) conditions are considered in the takeoff analysis, as well as a dry runway at sea level, non-icing conditions, no runway slope and no wind. In the takeoff modelling, flap and gear settings were also taken into account, as well as rolling friction and ground effect (see Section 2.3). In the OEI case, asymmetric rudder drag and propeller feathering drag were also modelled, as described in Section 2.4. Furthermore, part of the analysis was to verify that the altitude gradients during the second- and fourth-segment climb (see Figure 5) are above the specified values in CS-25.111 and

CS-25.121 [16], namely, 2.4% and 1.2% for the second segment and the fourth segment, respectively, for aircraft with one out of two engines inoperative.

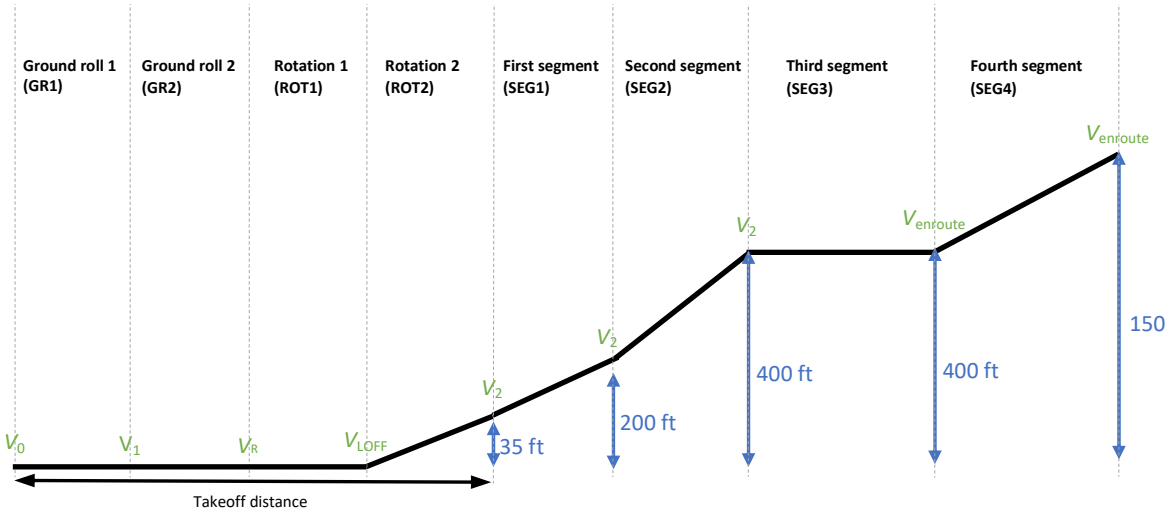

AEO

Segment	GR1	GR2	ROT1	ROT2	SEG1	SEG2	SEG3	SEG4
Gear	extended	extended	extended	extended	extended	retracted	retracted	retracted
Flaps	takeoff	takeoff	takeoff	takeoff	takeoff	takeoff	clean	clean
Power	normal takeoff AEO	normal takeoff AEO	normal takeoff AEO	normal takeoff AEO	normal takeoff AEO	normal takeoff AEO	normal takeoff AEO	maximum continuous AEO

OEI

Segment	GR1	GR2	ROT1	ROT2	SEG1	SEG2	SEG3	SEG4
Gear	extended	extended	extended	extended	extended	retracted	retracted	retracted
Flaps	takeoff	takeoff	takeoff	takeoff	takeoff	takeoff	clean	clean
Power	normal takeoff AEO	maximum takeoff OEI	maximum takeoff OEI	maximum takeoff OEI	maximum takeoff OEI	maximum takeoff OEI	maximum takeoff OEI	maximum continuous OEI

Figure 5. Division of the takeoff phase into segments determined by flap, landing gear and power settings.

2.3. Aircraft Equations of Motion

In the default simulation flow (see the black arrows in Figure 3), the aircraft model takes as input the flight path variables from the mission profile in combination with aircraft specific parameters (such as the aircraft mass, and lift and drag coefficients as functions of flap and gear settings and Mach number) and calculates the required thrust as a function of time. The model is based on a so-called "point mass" representation of the aircraft; see Figure 6.

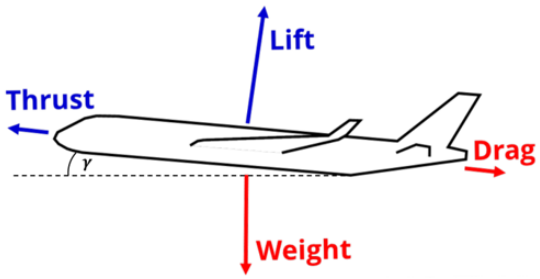

Figure 6. Illustration of the forces (drag, lift, weight and thrust) in the basic aerodynamic "point mass" model, with flight path angle γ.

Both flight and on-ground behavior have been modelled, taking into account normal forces and rolling friction as well as dependency of the aerodynamic coefficients on flap and gear settings. Only forward motion and flight path angle are included in the flight mission. Turns and maneuvers and roll and yaw rotations are not considered. Equations (1)–(9) below detail the calculation process of the thrust, with all variables dependent on time t. SI units are applicable. Changes in flight path angle γ are approximated by (piecewise) circular motion (see Equation (7)). The thrust T and flight path angle γ can be expressed by Equations (1) and (2):

$$T = m \cdot \dot{v} + D + D_{\text{ground}} + m \cdot g \cdot \sin\gamma, \tag{1}$$

$$\sin\gamma = \frac{\dot{h}}{v}, \tag{2}$$

where v is true air speed (TAS), h is altitude, g is gravitational acceleration, D and D_{ground} are drag forces (see Equations (4) and (5)), and m is aircraft instantaneous mass, which is calculated by Equation (3):

$$m(t) = m_{\text{TO}} - \int_0^t \dot{m}_{\text{fuel}} dt, \tag{3}$$

where m_{TO} is the takeoff mass and $\dot{m}_{fuel}$ is the fuel flow, which is computed using the engine or HPS model (see Equations (30) and (37) in Sections 2.6 and 2.7, respectively). The drag forces D and D_{ground} are calculated by

$$D = C_D \cdot \frac{1}{2}\rho \cdot v^2 \cdot S_{\text{w}}, \tag{4}$$

$$D_{\text{ground}} = \mu \cdot N, \tag{5}$$

where ρ is air density, S_{w} is total wing area (reference area), C_D is the aerodynamic drag coefficient (see Equation (9)), μ is the ground rolling friction coefficient (assumed equal to 0.03 [24]) and N is the normal force calculated by Equation (6):

$$N = \begin{cases} m \cdot g - \frac{1}{2}\rho \cdot v^2 \cdot S_{\text{w}} \cdot C_{L0}, & h = 0 \\ 0, & h > 0 \end{cases}, \tag{6}$$

where C_{L_0} is the lift coefficient at zero angle of attack (assumed equal to 0.12). The lift force L is expressed by Equation (7) and is used to derive the aerodynamic lift and drag coefficients C_L and C_D, which can be computed using Equations (8) and (9):

$$L = m \cdot v \cdot \dot{\gamma} + (m \cdot g - N) \cdot \cos\gamma, \tag{7}$$

$$C_L = {}^{L}/\left(\frac{1}{2}\rho \cdot v^2 \cdot S_{\text{w}}\right), \tag{8}$$

$$C_D = C_{D_0} + k{C_L}^2 + \Delta C_{D_{\text{flaps}}} + \Delta C_{D_{\text{gear}}} + \Delta C_{D_{\text{OEI}}}, \tag{9}$$

where C_{D_0} is the zero-lift drag coefficient, ΔC_{D_x} the drag coefficients dependent on flaps, gear and OEI settings (rudder drag to stabilize the aircraft during the OEI case and propeller feathering drag due to the inactive propeller of the failed engine), respectively, and k the lift-induced drag coefficient. The buildup of the drag coefficients is detailed in Section 2.4. The time derivatives $\dot{v}$, $\dot{h}$ and $\dot{\gamma}$ in Equations (1), (2) and (7) are approximated numerically.

If the alternative simulation model flow is chosen (see the orange arrows in Figure 3), the thrust T is specified in the equations of motion. The specified thrust T on its turn is calculated from the specified shaft power value (see Equation (24)) using the propeller performance model, which is described in Section 2.5. The accelerations and flightpath

angle are calculated in a segmented approach. During the horizontal flight segments—e.g., takeoff ground run—the flightpath angle is set to zero. The acceleration is calculated by rewriting Equation (1) as Equation (10):

$$\dot{v} = \frac{T - D - D_{\text{ground}}}{m}. \tag{10}$$

The TAS can then be derived by time integration of $\dot{v}$, in Equation (11):

$$v(t) = \int_0^t \dot{v} dt. \tag{11}$$

During the non-horizontal flight sections, the flightpath angle is calculated by rewriting Equation (1) as Equation (12):

$$\sin\gamma = \frac{T - m \cdot \dot{v} - D}{m \cdot g}. \tag{12}$$

In this case, either a constant velocity is assumed (zero acceleration) or the velocity is interpolated linearly with altitude, and $\dot{v}$ is then approximated numerically from v. The altitude is calculated by time integration of $\dot{h}$ combined with Equation (2), which results in Equation (13):

$$h = \int_0^t \dot{v} \cdot \sin\gamma \, dt. \tag{13}$$

In all cases, the horizontal distance x is calculated by time integration of the horizontal velocity by Equation (14):

$$x = \int_0^t v \cdot \cos\gamma dt. \tag{14}$$

2.4. Aerodynamic Coefficients

The aerodynamic coefficients of the aircraft lift-drag polar—as used in Equation (9)—were estimated by comparing information from various sources from the public domain. Drag polars from an ATR 42-related study by Gunnam [25] and a Dash 8-300-related study by Quillet et al. [26], and from conceptual design textbooks, Roskam averaged statistics [27] and a combination of Roskam and Obert [28] were compared. The coefficients—for the clean configuration without flap or gear contributions, in cruise conditions—are summarized in Table 2 below. The corresponding drag polars, depicted as lift-to-drag ratio as function of lift coefficient C_L—derived using Table 2 and Equations (4), (8) and (9)—are shown in Figure 7.

Table 2. Summary of compared drag polar coefficients (clean configuration, cruise condition).

Source	Zero-Lift Drag Coefficient C_{D_0} [−]	Lift-Induced Drag Coefficient k [−]
Gunnam [25]	0.0247	0.0312
Quillet et al. [26]	0.0322	0.0372
Roskam averaged statistics [27]	0.0210	0.0289
Roskam and Obert [28]	0.0306	0.0320

Figure 7 shows that the various drag polars have similar shapes, but the one provided by Quillet [26] has the lowest *L/D* prediction. In the remainder of this study, this polar was applied, following a worst-case estimation approach. No values of the clean configuration drag polar coefficients were found for operating conditions other than cruise (e.g., for lower

Reynolds numbers). Therefore, for simplicity, the clean configuration cruise drag polar coefficients were applied during all mission phases.

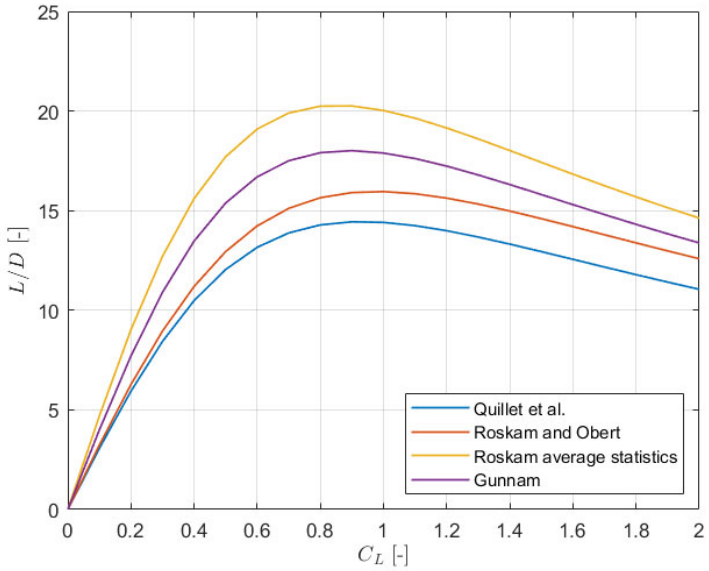

Figure 7. Comparison of drag polars (clean configuration) by lift-to-drag ratio *L/D* as function of lift coefficient C_L Quillet [26].

During takeoff, additional drag contributions of flaps and landing gear were taken into account. However, because these drag contributions were not provided in Ref. [26], the estimations provided by Roskam [27] were applied. The resulting coefficients for the clean and for the takeoff condition are summarized in Table 3 below.

Table 3. Clean and takeoff drag polar coefficients applied.

Aircraft Configuration	Zero-Lift Drag Coefficient C_{D_0} [−]	Lift-Induced Drag Coefficient k [−]
Clean	0.0322	0.0372
Takeoff flaps	0.0422	0.0403
Takeoff flaps + Landing gear	0.0572	0.0403

In the OEI case, the rudder must be deflected to stabilize the aircraft forward motion due to asymmetric thrust by the one engine that is still in operation. This creates additional drag. The "asymmetric rudder drag" contribution was estimated (based on in-house experience at NLR) by the empirical relation

$$\Delta C_{D_{\text{rud}}} = 0.07 \cdot {\delta_{\text{rud}}}^2, \tag{15}$$

with δ_{rud} the rudder deflection in radials. A maximum δ_{rud} value of 16 deg (0.28 rad) [29] was applied, for which Equation (15) leads to a $\Delta C_{D_{rud}}$ contribution of 0.0055. Furthermore, in the OEI case, the dysfunctional propeller will feather but still cause additional drag. To estimate the additional drag, a formula by Torenbeek [30] is used:

$$\Delta C_{D_{\text{prop}}} = \frac{0.00125\, B_{\text{p}}\, {D_{\text{p}}}^2}{S_{\text{w}}}, \tag{16}$$

where S_{w} is the wing surface area, B_{p} the number of propeller blades and D_{p} the propeller diameter. Inserting the values from Table 1 into Equation (16) results in a $\Delta C_{D_{\text{prop}}}$ of 0.0014.

As the takeoff is performed in close proximity to the ground, the ground effect is taken into account for performance calculations. The effects are expressed as ratios between, on one hand, the lift coefficient in ground effect (C_L) with respect to the lift coefficient in the absence of the ground effect ($C_{L\infty}$), and, on the other hand, the ratio between the lift-induced drag factor in ground effect (k_{eff}) and the lift-induced drag factor in absence of the ground effect (k). The ground effect on the lift coefficient is expressed using the $\frac{C_L}{C_{L\infty}}$ ratio by Torenbeek [30]; see Equation (17). The formula is simplified by assuming a straight wing (without sweep):

$$\frac{C_L}{C_{L\infty}} = 1 + \sigma - \frac{\sigma\, AR}{2 + \sqrt{AR^2 + 4}} - \frac{\beta}{4\,\pi \frac{h}{c_g}} \left(C_{L\infty} - \frac{C_{L\alpha}}{16 \frac{h}{c_g}} \right), \tag{17}$$

where h is the distance between the wing and the ground (for this purpose assumed to be similar as the modelled altitude), c_g is the mean geometric chord of the wing, B_w is the wing span, AR is the wing aspect ratio, σ is the ground effect factor, β is a correction factor for the ground effect and $C_{L\alpha}$ is the lift curve slope obtained from the thin airfoil theory formula; these are obtained from Equations (18)–(22):

$$C_{L\alpha} = \frac{2\pi}{1 + 2\pi\, k}, \tag{18}$$

$$\sigma = \exp\left\{ -2.48 \left(2\frac{h}{B_w} \right)^{0.768} \right\}, \tag{19}$$

$$\beta = \sqrt{1 + \left(2\frac{h}{B_w} \right)^2} - 2\frac{h}{b}, \tag{20}$$

$$AR = \frac{{B_w}^2}{S_w}, \tag{21}$$

$$c_g = \frac{S_w}{B_w}. \tag{22}$$

The ground effect on the drag coefficient is determined using the method by Raymer [31], for which the lift induced drag term—see also Equation (9)—is corrected with the factor $\frac{k_{eff}}{k}$.

$$\frac{k_{eff}}{k} = \frac{33 \left(\frac{h}{B_w} \right)^{1.5}}{1 + 33 \left(\frac{h}{B_w} \right)^{1.5}}, \tag{23}$$

Equations (17)–(23) show that when the altitude h becomes sufficiently large, the ratios $\frac{CL}{CL_\infty}$ and $\frac{k_{eff}}{k}$ get closer to 1.

Finally, as explained in Section 1, the HPS is retrofitted into the Dash 8-300 aircraft. Therefore, the aerodynamic coefficients that are applicable to the reference aircraft are also applicable to the H_2-electric configuration. Nevertheless, additional drag is expected from an increased nacelle size, taking into account the ram air ducts that are needed to cool the fuel cells. Detailed drag models were not available yet, due to the conceptual stage of the design. A simplified approach was adopted from Ref. [13], assuming that the zero-lift drag (C_{D_0}) is proportional to the frontal area of the aircraft. The frontal area increase (due to the cooling ducts) was estimated at 5% [13], by computing the required cooling air mass flows during takeoff in hot ambient conditions (35 °C), and corresponding duct sizes. During discussions with the author and with the HAPSS technical project coordinator [32], it was agreed to increase this percentage to 7%, following a more conservative approach. This

increase can be motivated by a lower FCS efficiency (and therefore more heat generation) than was assumed in Ref. [13]. Nevertheless, this 7% is still subject to uncertainty and needs to be refined during subsequent development phases of the HAPSS project.

2.5. Propeller Model

The thrust that is needed for the aircraft motion (see Equations (1), (10) and (12)) is delivered by a propeller. In case of the Dash 8-300, it is a Hamilton Sunstrand propeller with four blades, variable pitch and a maximum propeller shaft speed of 1212 rpm [19]. The relation between thrust and propeller shaft power was modelled by Equation (24):

$$T \cdot v = P_{\text{shaft}} \cdot \eta_{\text{prop}}, \tag{24}$$

where v is the true air speed, T the total net thrust, P_{shaft} the total mechanical shaft power and η_{prop} the propeller efficiency.

The propeller efficiency was modelled by reproducing the Dash 8-300 propeller map presented in Ref. [26]. In the propeller map, the propeller efficiency is given as function of advance ratio J and power coefficient C_{P}, by Equation (25) (the advance ratio J and power coefficient C_{P}, are expressed by Equations (26) and (27), respectively):

$$\eta_{\text{prop}} = \hat{f}(J, C_{\text{P}}), \tag{25}$$

$$J = \frac{v}{n \cdot D_{\text{p}}}, \tag{26}$$

$$C_{\text{P}} = \frac{P_{\text{shaft}}}{\rho \cdot n^3 \cdot {D_{\text{p}}}^5}, \tag{27}$$

where ρ is the air density in kg/m^3, n is the shaft speed in rev/s, D_{p} is the propeller diameter in m and $\hat{f}$ is the lookup table interpolation function, as illustrated in Figure 8.

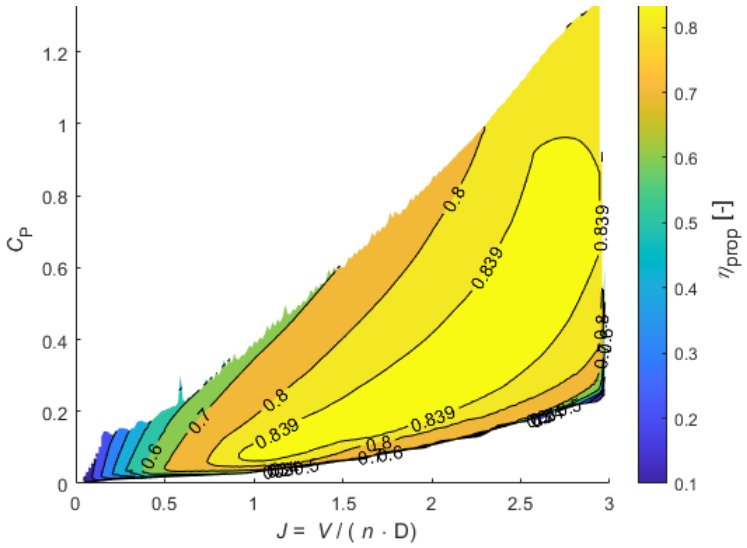

Figure 8. Depiction of the Dash 8-300 propeller map $\eta_{\text{prop}} = \hat{f}(J, C_{\text{P}})$, reproduced from Ref. [26].

For situations where shaft power should be computed for a known thrust, a second propeller map is constructed, which gives the propeller efficiency as a function of advance ratio J and thrust coefficient C_{T}, by Equations (28) and (29):

$$\eta_{\text{prop}} = \hat{g}(J, C_{\text{T}}), \tag{28}$$

$$C_T = \frac{T}{\rho \cdot n^2 \cdot {D_p}^4} = \frac{\eta_{prop} \cdot C_P}{J}, \tag{29}$$

where $\hat{g}$ is the lookup table interpolation function, as illustrated in Figure 9.

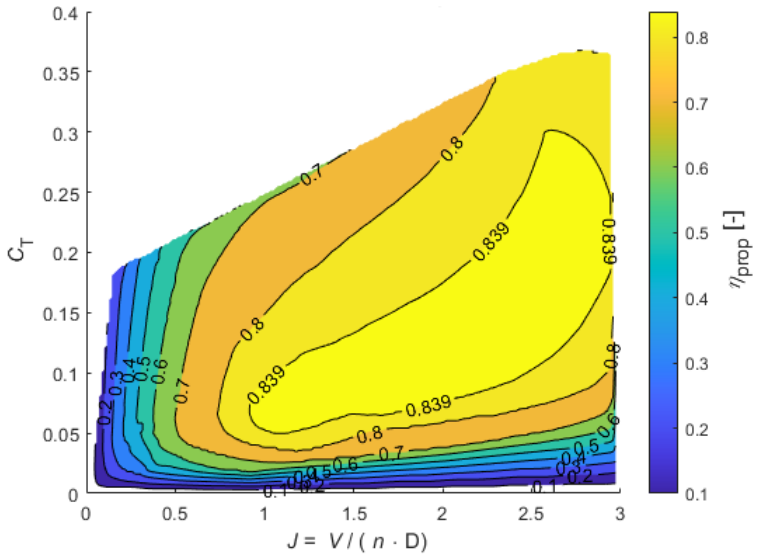

Figure 9. Depiction of the Dash 8-300 propeller map $\eta_{prop} = \hat{g}(J, C_T)$.

2.6. Engine Model

In the reference aircraft, the shaft power is delivered by a PW123 turboprop engine. A maximum shaft power of 1775 kW per engine can be provided [20].

The engine model depicted in Figure 3 was used to predict fuel flow as function of shaft power and flight conditions. The fuel flow (used in Equation (3)) can be predicted by means of the Power Specific Fuel Consumption (PSFC) number

$$\dot{m}_{fuel} = PSFC \cdot P_{shaft}. \tag{30}$$

The PSFC depends on the actual flight condition. For the PW123 engine, a PSFC during takeoff of 0.286 kg/kWh was found [33]. The PSFC values in the other flight phases were modelled by using an in-house data set of a similar turboprop engine and scaling it with the takeoff PSFC value. Typical values are listed in Table 4.

Table 4. Modelled fuel flow and PSFC values for typical mission operating points.

Mission Phase	h [m]	v [m/s]	P_{shaft} (1 Engine) [kW]	$\dot{m}_{fuel}$ (1 Engine) [kg/h]	*PSFC* [kg/kWh]
taxi	0	10	100	86	0.860
take off	0	0	1775	507	0.285
climb	4000	100	1603	462	0.288
cruise	7620	133	1062	301	0.284
descent	4000	100	100	62	0.615
landing	0	0	855	267	0.321

2.7. HPS Model

In the simulations with the HPS retrofitted aircraft, the gas turbine engine model was replaced by an electric propulsion unit (EPU) and FCS performance model. The applied models are described in Sections 2.7.1 and 2.7.2.

The EPU and FCS are connected by an electric (DC) distribution system. Figure 10 depicts the applied architecture of the HPS, in a simplified way. The EPUs of the two propeller shafts are powered by four FCS modules. The DC buses of the EPUs are cross-connected: if one FCS module fails, the other three can still provide power and divide it over the two shafts.

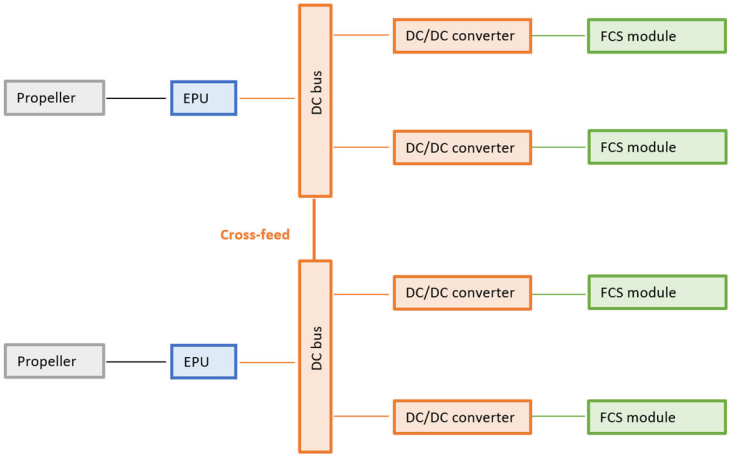

Figure 10. Illustrating scheme of HPS architecture, with four FCS modules.

In Ref. [13], batteries are also considered as part of the system architecture, e.g., to provide transient power demands. In our study, they were not modelled, as transient system responses were not considered.

2.7.1. EPU Model

The EPU [13] consists of the electric motor (EM), inverter and reduction gearbox (RGB) and delivers shaft power to the propeller. The EPU model describes the power losses by means of efficiencies. Electric power losses in the electric distribution system (e.g., cables and DC-DC converters) are also included. Furthermore, the power offtakes needed for the non-propulsive systems (e.g., ice protection system, environmental control system, flight controls, avionics and EPU cooling) are taken into account. For simplicity, all these losses and the power offtakes are embedded in the EPU model. The model (see Equation (31)) describes the relation between propeller shaft power to be delivered and the corresponding electric DC power demand to be delivered by the FCS:

$$P_{\text{shaft}} = \eta_{\text{EPU}} \cdot (P_{\text{FCS,out}} - P_{\text{offtakes}}), \tag{31}$$

where η_{EPU}—estimated at 88%—represents the multiplied efficiencies, taking into account the power losses at the RGB, motor, inverter and electric distribution system. The variable P_{offtakes} in Equation (31) represents the power needed for the offtakes, which ranges between 1% and 4% of the shaft power, depending on the flight phase [13].

2.7.2. Fuel Cell System Model

The FCS consists of the fuel cell (FC) stack and balance of plant (BoP) components. The FC stack generates the electric power (by means of oxidation of supplied H_2). The BoP components are needed to provide the optimal operating conditions of the FC stack in terms of air supply mass flow, pressure, temperature and humidity. Furthermore, the FC stack must be cooled. In our FCS model, the considered BoP components are as follows:

- A compressor that is needed to deliver the air mass flow, at the pressure needed by the FC stack;

- A heat exchanger to lower the air temperature—which increases due to the compressor—to the temperature level needed by the FC stack;
- A humidifier that creates the level of air humidity needed by the FC stack.

The power consumption of the TMS that removes all of the heat generated by the FCS components is addressed as well. The FCS model is shown schematically in Figure 11.

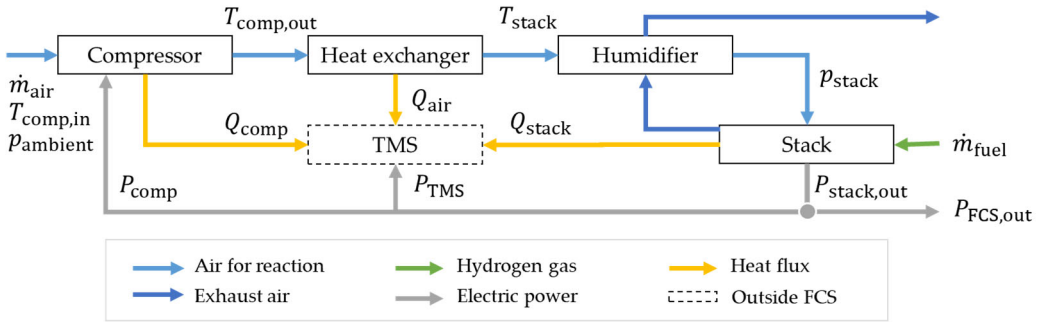

Figure 11. Illustrating scheme of the FCS model.

The FCS model describes the relation between DC output power $P_{FCS,out}$ and H_2 fuel flow $\dot{m}_{fuel}$

$$P_{FCS,out} = \eta_{FCS,HHV} \cdot \dot{m}_{fuel} \cdot HHV_{H_2}, \tag{32}$$

where HHV_{H_2} represents the Higher Heating Value of H_2 (142 MJ/kg) and $\eta_{FCS,HHV}$ represents the overall FCS efficiency with respect to the HHV. In this paper, the HHV is used instead of the Lower Heating Value (LHV) [34,35], since the fuel cell reaction will result in liquid water (operating temperature below 100 °C), and the condensation heat must be taken into account for FC stack cooling.

In Equation (32), $\eta_{FCS,HHV}$ and $\dot{m}_{fuel}$ cannot be computed directly for a desired $P_{FCS,out}$, but can be computed for a given $P_{stack,out}$, the FC stack output. Rather than employing an iterative method to find the $P_{stack,out}$ that leads to the desired $P_{FCS,out}$, values of $P_{FCS,out}$, $\dot{m}_{fuel}$ and $\eta_{FCS,HHV}$ are pre-computed for a range of $P_{stack,out}$ values (using Equations (36)–(44)), and the results are interpolated.

The FC stack design was outside the scope of this work. The FC stack model was based on measurement data from an ElringKlinger fuel cell [34]. The measurements were performed using a stoichiometry factor of 1.7 and a range of operating pressures. Typical operating pressures for fuel cell stacks lie in range of 1.6 bar(a) to 1.9 bar(a) [35]. An FC stack pressure p_{stack} of 1.6 bar(a) (constant throughout the mission) was assumed in this paper. The operating temperature corresponding to that pressure in the measurements presented in Ref. [34] is 81 °C. Figure 12 plots the cell voltage U_{cell}, as a function of the current per unit area (the current density j). Furthermore, it shows the power density pd, which is defined by Equation (33) and can be calculated from Equation (34):

$$pd = \frac{P_{stack,out}}{A_{cells}}, \tag{33}$$

$$pd = U_{cell} \cdot j, \tag{34}$$

where A_{cells} is the total area of the cells. From the measurements in Ref [34] and the selected operating conditions, a maximum achievable pd of 0.93 W/cm^2 was found. Hence, the required total area of the cells A_{cells} can be determined (see Equation (35)) from the maximum needed stack output power $P_{stack,out,max}$ and the maximum power density pd_{max}:

$$A_{cells} = \frac{P_{stack,out,max}}{pd_{max}}. \tag{35}$$

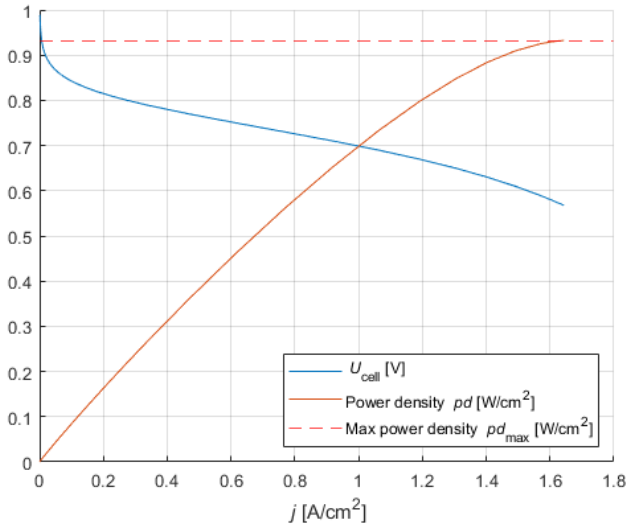

Figure 12. Curve relating current density j to cell voltage U_{cell} and power density pd. Based on measurements on an ElringKlinger stack at 1.6 bar(a) with a stoichiometry factor of 1.7 and temperature of 81 °C, derived from Ref. [34].

The efficiency of the fuel cell (relative to the HHV) $\eta_{\text{FC,HHV}}$ and the fuel consumption follow from Equations (36) and (37) [36]:

$$\eta_{\text{FC,HHV}} = \frac{U_{\text{cell}}}{U_{\text{cell,ref,HHV}}}, \tag{36}$$

$$\dot{m}_{\text{fuel}} = \frac{P_{\text{stack,out}}}{\eta_{\text{FC,HHV}} \cdot HHV_{\text{H}_2}}, \tag{37}$$

where $U_{\text{cell,ref,HHV}}$ is the cell reference voltage with respect to the HHV, 1.48 V [36].

It was assumed that the compressor will be electrically driven and use a (small) part of the electric power delivered by the FC stack. The compressor power depends on the FC stack pressure p_{stack} and the pressure losses in the air filter, heat exchanger and the humidifier. The pressure losses for various components that were assumed are specified in Table 5. The compressor power was modelled (in a simplified way) by

$$P_{\text{comp}} = \dot{m}_{\text{air}} \cdot c_{\text{p}} \cdot \left(T_{\text{comp,out}} - T_{\text{comp,in}}\right) \cdot \frac{1}{\eta_{\text{driver}}}, \tag{38}$$

$$T_{\text{comp,out}} = T_{\text{comp,in}} \cdot \left(1 + \frac{PR^{\frac{\gamma-1}{\gamma}} - 1}{\eta_{\text{is}}}\right), \tag{39}$$

where $\dot{m}_{\text{air}}$ represents the air mass flow (derived from the H_2 fuel flow and stoichiometry factor), c_{p} the specific heat capacity, γ the ratio of the specific heat capacities, η_{is} the isentropic efficiency and η_{driver} the driver efficiency (motor bearings, etc.). The values used can be found in Table 5. In Equations (38) and (39), $T_{\text{comp,in}}$ and $T_{\text{comp,out}}$ represent the total temperature at the compressor inlet and outlet, respectively, and PR represents the compressor pressure ratio. As a simplification, the ram air compression effect in the FC stack air intake was ignored, and the compressor is used for the compression from static ambient ISA atmosphere temperature (T_{ambient}) and pressure (p_{ambient}) to the required pressure. This simplification (conservatively) overestimates the required compressor power, especially at higher Mach numbers. For cruise at Mach 0.43, the overestimation of the compressor power is ca 10%. Since the compressor power itself is ca. 10% of the FC stack power during cruise, the error in FCS output power is ca. 1%. For low Mach numbers, the

error is significantly lower: at lift-off, the overestimation of the compressor power is ca. 2% and the FCS output power error is ca. 0.1%. The advantage of the simplification is that it eliminates the dependency of the FCS model on flight velocity, greatly reducing the number of iterations (computational cost) needed to create the lookup tables for interpolation.

Table 5. FCS model parameters.

Parameter	Symbol	Value
Air filter pressure drop [34]	-	500 Pa
Humidifier pressure drop (supply side) [34]	-	5000 Pa
Heat exchanger pressure drop (supply side) [34]	-	10,000 Pa
Specific heat capacity (for air)	c_p	1006 J/kg/K
Ratio of the specific heat capacities (for air)	γ	1.4
Compressor isentropic efficiency [35]	η_{is}	0.76
Compressor driver efficiency (mechanical, electrical and power conversion efficiency) [35]	η_{driver}	$0.97 \times 0.94 \times 0.95 = 0.87$

The heat exchanger model—describing heat to be removed from the compressed air—is shown below in Equation (42). Furthermore, a fixed pressure drop was assumed for the heat exchanger (see Table 5).

For the humidifier, only a fixed pressure drop was modelled (see Table 5). The air humidity itself is not taken into account in this FCS model.

The TMS coolant pump power (P_{TMS}), needed to cool the FCS components is modelled as follows. First, the total FCS heat rate to be cooled is computed as the sum of the heat rates (see Equation (40)):

- $\dot{Q}_{stack}$, defined as the loss between fuel power and FC stack output power (see Equation (41));
- $\dot{Q}_{air}$, defined as the extracted heat rate to cool the compressed air to the temperature level needed by the FC stack (see Equation (42));
- $\dot{Q}_{comp}$, defined as compressor driver power losses (e.g., inverter, motor, bearings) (see Equation (43)).

$$\dot{Q} = \dot{Q}_{stack} + \dot{Q}_{air} + \dot{Q}_{comp}, \tag{40}$$

$$\dot{Q}_{stack} = \dot{m}_{fuel} \cdot HHV_{H_2} - P_{stack,out}, \tag{41}$$

$$\dot{Q}_{air} = \left(T_{comp,out} - T_{stack}\right) \cdot \dot{m}_{air} \cdot c_p, \tag{42}$$

$$\dot{Q}_{comp} = (1 - \eta_{driver}) \cdot P_{comp}, \tag{43}$$

The TMS coolant pump power P_{TMS} is modelled as 2% of the heat rate to be cooled, based on inhouse experience [37]. Note that the drag of the TMS ram air ducts is accounted for in the aerodynamic model (see Section 2.4). The residual thrust from the exhaust is ignored and the potential for power recovery with a turbine is not considered in this study. Furthermore, it should be remarked that the EPU also needs cooling; however, in the context of this paper, it was assumed that the EPU is cooled by a separate system.

Finally, the FCS output power follows from Equation (44):

$$P_{FCS,out} = P_{stack,out} - P_{comp} - P_{TMS}. \tag{44}$$

In Ref. [34], a maximum achievable FCS output power was found for different altitudes. This limit is caused by a combination of operating limits of the applied FC stack (e.g.,

feasible air mass flow for various operating pressures) and the applied compressor (e.g., surge, choke and speed limits). Detailed modelling of the operating limits (see Ref. [34]) was out of scope of this paper. Instead, the resulting power limit—on the FCS level—was adopted from Ref. [34], in a scaled way: it was assumed that the maximum achievable FCS output power is proportional to the rated FCS output power (at sea level).

Figure 13 depicts the derived FCS efficiency model, as a function of altitude and FCS output power, relative to rated FCS output power. The latter refers to the maximum net useful (DC) output power of the FCS, at sea level ISA conditions, at the "end-of-life" condition. BoP power losses (e.g., compressor power) are already subtracted; see Equation (44). Figure 13 shows that the overall FCS efficiency decreases with altitude and with power demand.

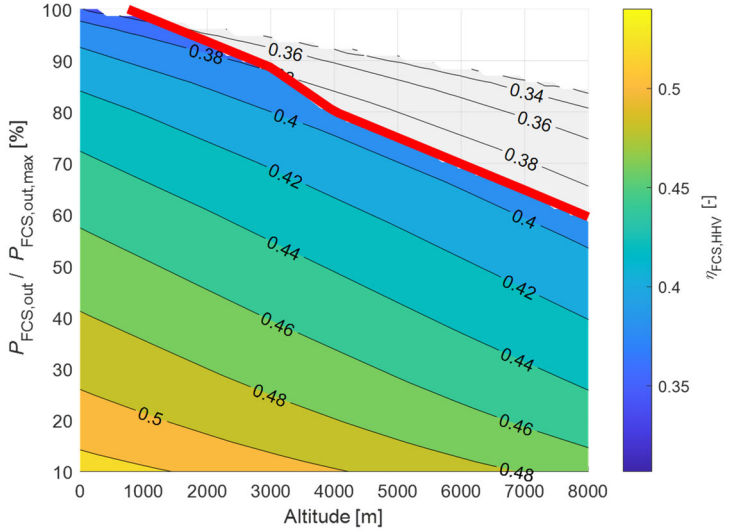

Figure 13. Derived FCS efficiency model, as a function of altitude and output power demand. In red, the altitude-dependent maximum system power limit from Ref. [34] is indicated.

Detailed mass estimations of the FCS are out of scope of this paper. Ref. [13] estimates an FCS specific power ($\overline{p}_{FCS}$) of 1.7 kW/kg. With this value, the FCS mass can be estimated using Equation (45):

$$P_{FCS,out} = \overline{p}_{FCS} \cdot m_{FCS}. \quad (45)$$

3. Results

The section presents the results of the performance simulations during critical mission phases. The first part describes the takeoff performance results. In the second part, the performance during climb, cruise and go-around is described.

3.1. Takeoff Performance

In this section, only the takeoff conditions for the OEI cases are presented, as these cases represent the critical performances.

3.1.1. Validation with Reference Aircraft Data

As a first step, takeoff simulations were performed with the reference aircraft model, for comparison with reference data. In Ref. [17], information on takeoff distances (TOD) was found for the reference aircraft. A takeoff with OEI was simulated: when the aircraft has reached decision speed v_1, one engine fails, and the takeoff proceeds in the OEI condition. The TOD represents the distance from takeoff start to the point where the 35 ft (10.7 m) clearance altitude is reached; see also Figure 5. A dry runway, non-icing conditions, no

runway slope and no wind are applicable. ISA sea level conditions were used. Figure 14 shows the results for the TOD segment. The simulation starts with normal takeoff (NTO) power of ~1600 kW per engine, which adds to ~3200 kW in total [20]. After the engine failure at v_1, the remaining operating engine is switched to a maximum takeoff (MTO) power setting (1775 kW). This results in a TOD of 1767 m. This simulation was performed with a takeoff mass (TOM) of 19.5 t, which is the maximum TOM of the reference aircraft (see Table 1). The simulation was repeated for various TOM values. The resulting predicted TOD values were compared with the corresponding data in Ref. [17]. The comparison results are shown in Figure 15. It can be seen in Figure 15 that for the lower TOM values, the simulated TODs match well with the data from [17]. For the larger TOM values, the simulation predictions overestimate the TOD data by up to 11%.

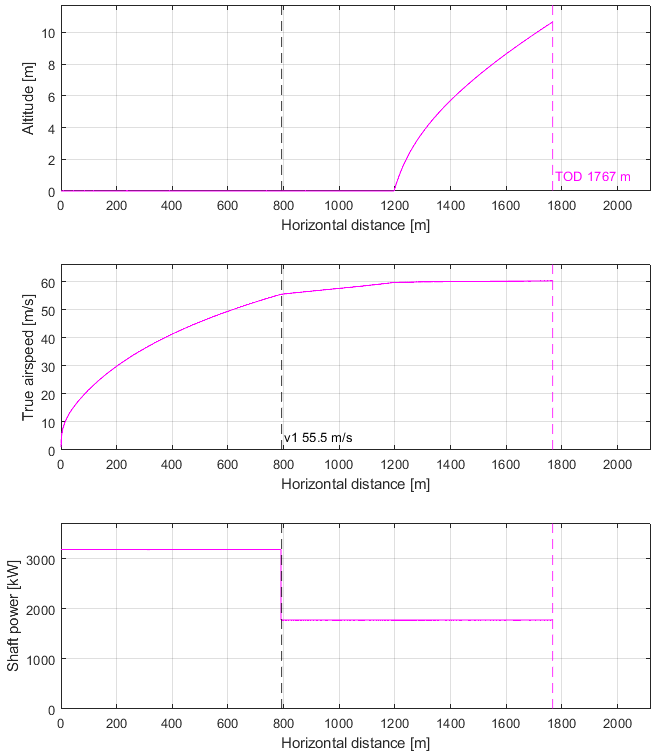

Figure 14. TOD segment simulation results with the reference aircraft.

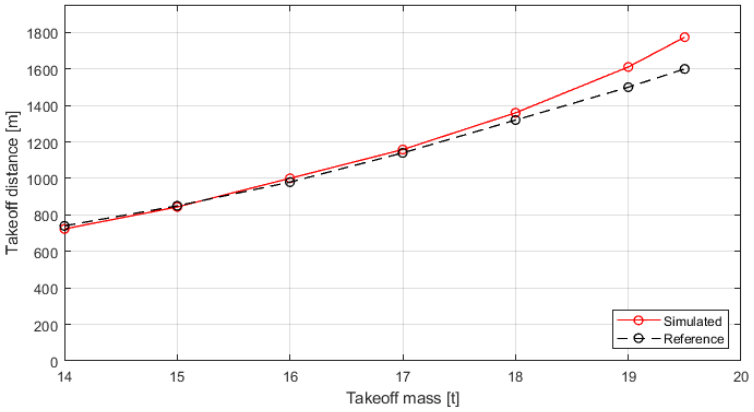

Figure 15. Comparison of simulated and reference takeoff distances [17] at ISA sea level conditions.

3.1.2. HAPSS Aircraft Results

Second, the takeoff phase (with OEI) was simulated with the HAPSS aircraft model, under the same conditions as with the reference aircraft (ISA, dry runway etc.). The TOM

was reduced from 19.5 t to 19.1 t (following the assumptions in Section 2.1). The parasite drag coefficient C_{D_0} of the aircraft increases by 7% (see Section 2.4). From Figure 10, it can be deduced that the most critical failure of a single component is the case where one propeller (or EPU) fails, rather than one FCS module. In that case, only the maximum shaft power that is allowed by the other propeller can be used. The propeller failure is therefore considered the OEI case for the HAPSS aircraft. Initially, the same MTO shaft power as with the reference aircraft was applied: 1775 kW. Figure 16 shows that this MTO power is not sufficient to achieve the 2.4% gradient requirement [16] during the second segment climb. An MTO shaft power of at least 1865 kW is needed to fulfill this requirement. Figure 16 also shows that both MTO power levels are more than sufficient to achieve the 1.2% gradient requirement [16] during the fourth-segment climb. It should be noted that the MTO power was maintained until the end of the takeoff phase. For the HPS, there are no time restrictions to maintain maximum power. However, in the case of the reference aircraft, MTO power to be provided by the engine would be time-restricted [20], and therefore the fourth-segment climb would be performed with a (lower) maximum continuous (MCT) power setting, as specified in Figure 5.

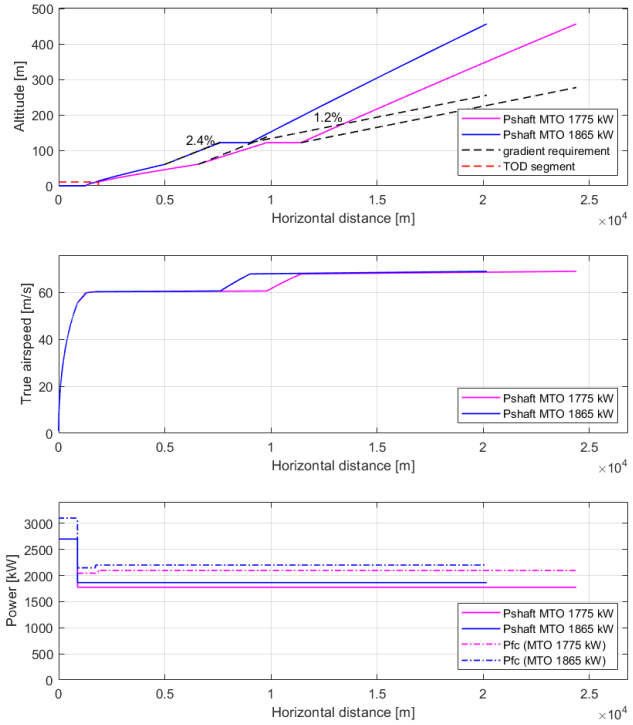

Figure 16. Takeoff simulation results with the HAPSS aircraft model for the OEI case.

Figure 17 zooms in on the first part of the takeoff phase–until the 35 ft (10.7 m) clearance altitude is reached–and shows that a TOD of 1838 m and 1717 m can be achieved with the 1775 kW and 1865 kW MTO power settings, respectively.

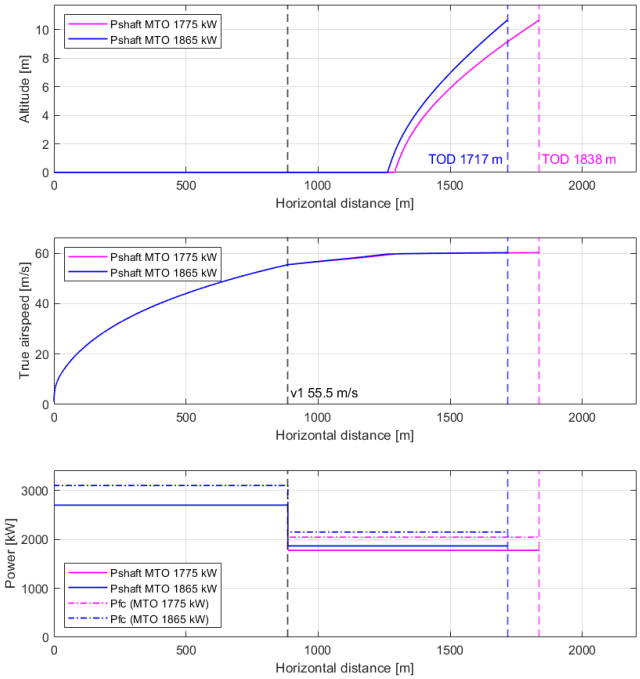

Figure 17. Takeoff distance segment simulation results with the HAPSS aircraft model for the OEI case.

This takeoff simulation was performed with a total rated FCS (output) power of 3.1 MW (see Section 2.7.2). This results in a total available propeller shaft power of 2.7 MW during the first part of the takeoff, when both propellers are still in operation, as can be seen in Figure 16. After the propeller failure, it is assumed that at least one FCS module on this propeller side is still operative and can provide electric power to the other side, facilitated by the cross-connected DC buses (see Figure 10).

3.1.3. Sensitivity Analysis of HAPSS Aircraft Parameters

The performance model still contains many uncertainties because several parameters were estimated, such as the parasite drag coefficient C_{D_0}, induced drag coefficient k, ground roll friction coefficient μ and propeller efficiency η_{prop}. Therefore, a sensitivity analysis was applied to better understand their impact on the predicted TOD and second-segment climb gradient (in case of OEI). In addition, the takeoff speed values (v_1, v_R, v_{LOFF}, v_2) were varied to estimate their impact on the takeoff distance and second-segment climb gradient. For all parameters, deviations from the reference values were applied, from -10% to $+10\%$, in separate cases. The exception is the propeller efficiency, which has -5% as a lower bound. The reason for this is that at the beginning of the takeoff, the propeller efficiency is already very low. When lowering it by more than 5%, the propeller model (see Section 2.5) goes outside the operating limits of the propeller map. Quadratic polynomials were fitted to the lower, upper bound and reference values, to predict the sensitivity behavior in between the bounds for each parameter. The results are depicted in Figure 18. The propeller efficiency has the largest impact (both on TOD and second-segment gradient). The induced drag factor k has the second-largest impact and C_{D_0} has the third-largest impact. Increased velocities (v_1, v_R, v_{LOFF}, v_2) have a large impact on TOD but a small impact on the gradient.

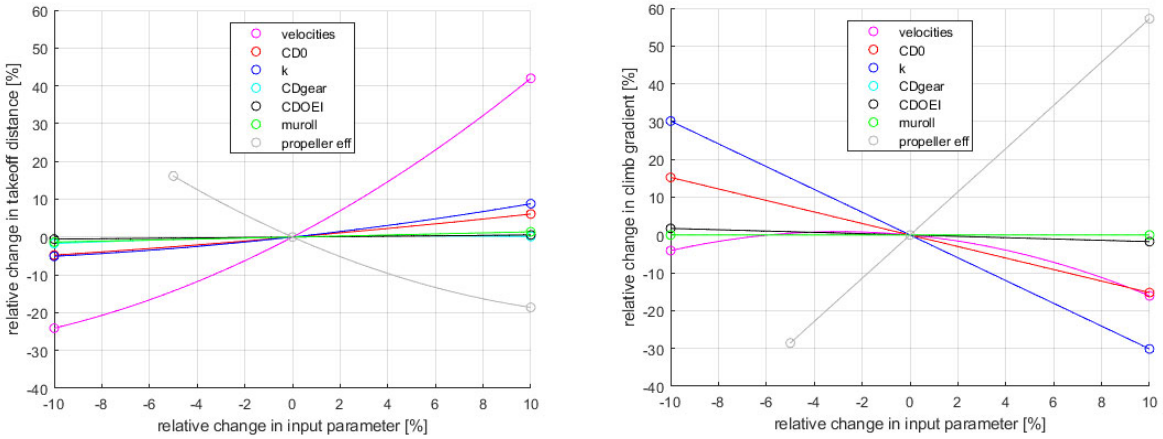

Figure 18. Sensitivity results for the takeoff distance (**left**) and second segment gradient (**right**) for various model parameters (expressed as percentage deviation from the reference value).

3.1.4. Effect of Gradual Power Increase on Fuel Cell Cooling Demand

During the takeoff analyses, full NTO power was applied immediately from the start of the takeoff phase (see the bottom plots of Figures 16 and 17). Applying full FCS power at the beginning of takeoff can be very demanding for the cooling of the FCS, due to the low air speed. Therefore, the effect of gradually increasing the power from the start of the takeoff was also investigated; see Figure 19.

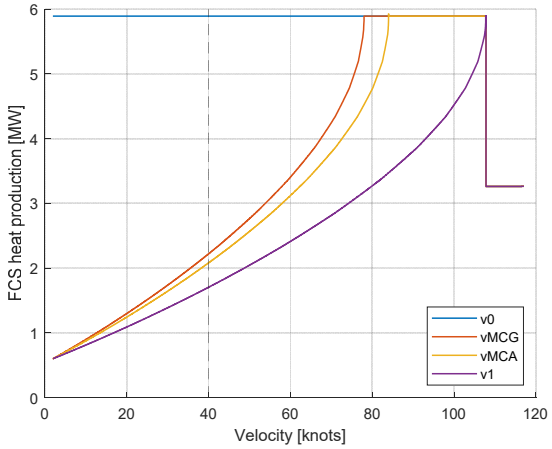

Figure 19. Fuel cell system heat production for different speeds at which the NTO shaft power is reached.

The FCS power was increased from 20% to 100% of the maximum NTO power, reaching that maximum at different speeds: either at the start of takeoff (v_0), at the ground minimum control speed (v_{MCG}), at the air minimum control speed (v_{MCA}) or at decision speed (v_1). The impact on TOD—while applying the OEI condition after v_1 was reached with MTO power 1865 kW—and fuel cell cooling demand was simulated. The latter is derived using Equation (40) and shown in Figure 19. Table 6 summarizes the results, where the cooling demand was evaluated at the (arbitrary) speed of 40 kts (20.6 m/s). The cases with gradually increased power reduce the cooling demand at 40 kts by at least 62% but result in a TOD increase of 9 to 20%.

Table 6. Speed at which max takeoff power is reached with corresponding impact on TOD and cooling demand.

Speed Cases (at Which Max Power Is Reached)	Speed Case Value [kts]	TOD [m], Determined by OEI Condition	Cooling Demand [MW] (at v = 40 kts)
from the start (reference case v_0)	0	1740	5.89
ground minimum control speed v_{MCG}	78	1890	2.22
air minimum control speed v_{MCA}	84	1920	2.08
decision speed v_1	108	2090	1.70

The investigated cases have no effect on the second-segment climb gradient, as in this segment, the same MTO power setting is applied, similarly to the previous takeoff analyses.

3.2. Performance During Other Mission Phases

3.2.1. Go-Around Performance

With a similar approach as with the takeoff analyses, the go-around (or missed approach) mission phase was analyzed. During the final approach phase, the aircraft switches to takeoff power settings, with OEI. During go-around, CS-25 [16] requires a minimum 2.1% climb gradient in the OEI case. Similarly to the takeoff case, this value could be achieved with the 1865 kW shaft power (one propeller) but not with the 1775 kW shaft power, as is illustrated in Figure 20.

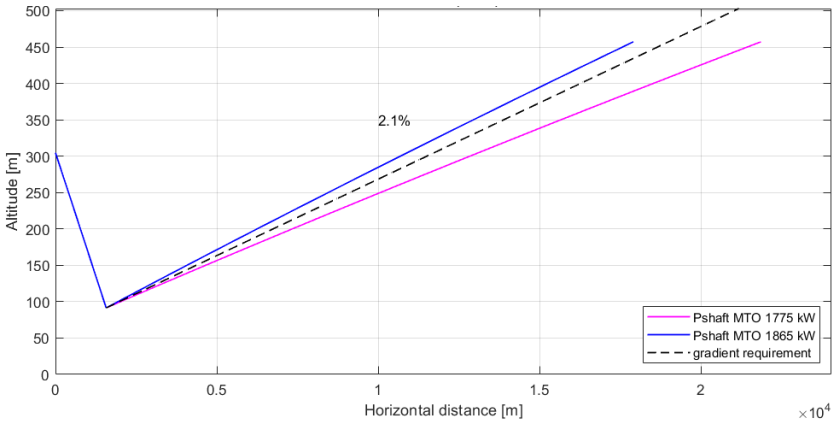

Figure 20. Go-around simulation results with the HAPSS aircraft model (OEI case) illustrating the gradient requirement.

3.2.2. Climb Performance

Contrary to the takeoff phase, no hard requirements were available for the climb phase to determine the minimum required FCS rated power. Instead, the example mission ROC profile for the reference aircraft (see Figure 4, taken from Ref. [22]) was used to evaluate the maximum rate of climb of three HAPSS aircraft variants with different FCS size in Figure 21. The black dashed line depicts the example ROC profile and serves as a reference.

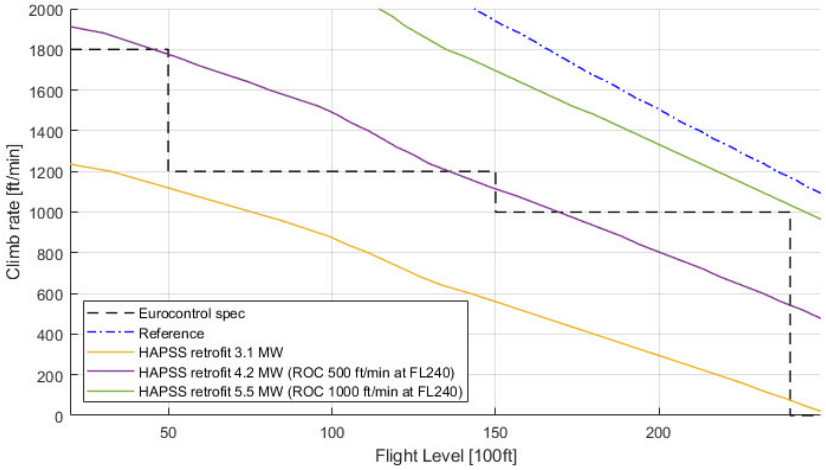

Figure 21. Climb performance plots for various FCS rated powers, compared with reference aircraft data.

The first selected FCS size (yellow curve in Figure 21) is identical to the FCS with 3.1 MW-rated power, as determined in the previous section. This FCS can, in theory, fly to flight level (FL) 240 (24,000 ft, 7315 m altitude), but at a very slow climb rate. The total climb to FL240 would take more than 1 h. In the example mission profile of the reference aircraft, the total climb to FL240 takes only 20 min. The second FCS—which has a larger rated power (4.2 MW; purple curve) and will therefore be larger and heavier—can follow the reference mission profile up to FL140 and is able to achieve a maximum climb rate of 500 ft/min at FL240, which is about half the climb speed at that altitude in the example mission profile. The third (even larger) FCS (5.5 MW; green curve) is able to follow the typical mission profile with a maximum climb rate of 1000 ft/min at FL240. This FCS is required for a comparable climb performance to the reference aircraft (dash-dotted blue line), in terms of maximum rate of climb at higher altitude.

The effect of the different FCS power ratings on the mass can be estimated using Equation (45). Table 7 summarizes the tradeoff of FCS rated power with the available payload mass, taking into account a fixed MTOM of 19.1 t (see Table 1) and a fixed LH_2 fuel and tank mass. For comparison, the initially sized FCS [13] (that corresponds with the design payload mass of 3.1 t) has been added as well, presented in italics format in Table 7.

Table 7. Tradeoff values between FCS rated power and payload, for a fixed MTOM (19.1 t) and fixed FCS specific power (1.7 kW/kg [13]).

Rated FCS Power [MW]	Estimated FCS Mass [t]	Payload Mass [t]	Comment
3.7	*2.2*	*3.1*	*Based on [13]*
3.1	1.8	3.4	Sized for takeoff
4.2	2.5	2.8	ROC@FL240 500 ft/min
5.5	3.2	2.0	ROC@FL240 1000 ft/min

3.2.3. Cruise Performance

Finally, the cruise performance of the HAPSS aircraft was analyzed. Using the 3.1 MW-rated FCS, several cruise altitude and speed settings were varied, to explore the effect on the energy efficiency. Figure 22 illustrates the exploration results in terms of range-specific energy consumption (RSEC) in MJ/km. It also shows the range-optimal altitude for each

speed (marked by the red curve). This is the altitude for a given speed at which the fuel flow is lowest and the potential range therefore maximal. For comparison, the same exploration was also performed with the reference aircraft. The RSEC is calculated for each potential cruise altitude–speed combination, by dividing the cruise fuel flow by the corresponding air speed and multiplying it by the LHV (for the reference aircraft) or the HHV (for the HAPSS aircraft). The RSEC is impacted by the aerodynamic efficiency (*L/D*), propeller efficiency and HPS efficiency (of the HAPSS aircraft) or gas turbine efficiency (of the reference aircraft). For the HAPSS aircraft, the RSEC increases with altitude, which is mainly caused by the lower FCS efficiency at altitude, see Figure 13. For the reference aircraft, it is the other way around: the gas turbine operates more efficiently at higher altitudes. For both aircraft, the RSEC contours also show symmetry with respect to the speed values. This is because *L/D* is optimal for a particular lift coefficient C_L (as can be seen in Figure 7). The cruise lift coefficient, in turn, is impacted by the speed and altitude (see Equation 8).

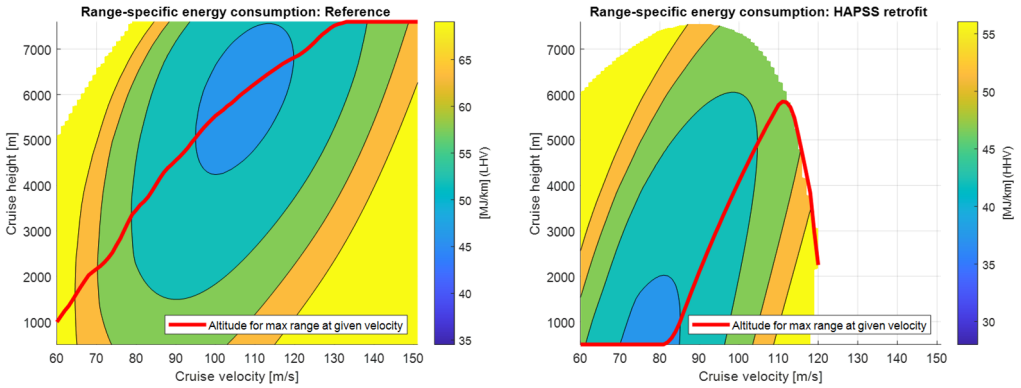

Figure 22. RSEC for various cruise altitudes and speed conditions, for the reference kerosene aircraft (**left**) and the HAPSS aircraft (**right**).

Figure 22 also provides information on the operating limits. It shows that with the 3.1 MW-rated FCS, cruising at the Dash 8-300 ceiling altitude of 25,000 ft (7620 m) with a TAS of 133 m/s (see Table 1) is not feasible (a service ceiling of 7620 m was found to be possible with the 3.1 MW-rated FCS, but at the expense of higher fuel consumption and slower speed, which is operationally not beneficial). The FCS output power limit (see Section 2.7.2) causes the visible operating limits. Following the red line in the right part of Figure 22 shows that an optimal cruise performance (in terms of high range and high TAS) is achieved at 112 m/s and 5800 m. Larger TAS values are feasible, but due to the operating limits, the HAPSS aircraft is forced to fly lower, which causes a decrease in *L/D* and therefore a sharp increase in RSEC. In general, following the red line in the right graph of Figure 22 shows that flying lower and slower decreases the RSEC, in the HAPSS aircraft case.

When comparing the left and right graph of Figure 22, one can see that the overall RSEC values of the HAPSS aircraft are slightly lower. This can be explained by the differences in powertrain efficiency. The reference aircraft has a typical cruise PSFC of 0.284 kg/kWh (see Table 4), which corresponds to an overall powertrain efficiency (from fuel power to shaft power) of ~30%. In cruise condition, the HAPSS aircraft has a minimal FCS efficiency of ~39% (see Figure 13). Taking into account the EPU losses, this results in a minimal overall powertrain efficiency of ~34%. This efficiency increase still compensates for the drag increase due to the TMS (estimated at 7% increase in C_{D_0}; see Section 2.4), as the efficiency increase from 30% to 34% is more than 7% (relatively: 34/30 > 1.07).

4. Discussion

In this section, the results (see the previous section) are discussed in relation to the underlying models, methods and assumptions. Modelling limitations, potential improvements and directions for future research are suggested and summarized in Table 8.

In the results section, it was shown that the performance models overestimate the TOD with 11% for the MTOM case of the reference aircraft. This overestimation could be (partly) due to the relatively "pessimistic" setting of the aerodynamic coefficients (see Section 2.4). The sensitivity analysis described in Section 3.1.3 shows that a 10% decrease in induced drag coefficient k results in ~5% lower TOD. It should be noted that this sensitivity analysis was performed with the HAPSS aircraft. However, the lift induced drag coefficient was not changed between reference and HAPSS aircraft.

The TOD overestimation could also be (partly) explained by a (small) level of exhaust thrust that the gas turbine engine produces during takeoff [38], which could be implicit to the lower TOD values stated in Ref. [17], but which was not taken into account in the TOD simulation.

The values stated in Ref. [17], to which the simulated TOD were compared, are in fact takeoff field length (TOFL) values. The TOFL [16] is the maximum of the TOD and the accelerate–stop distance: the total distance needed to accelerate to v_1 and then decelerate to full stop, in the case that the pilot chooses to reject the takeoff after engine failure. The accelerate–stop case was not simulated in this study. However, given that the TOD estimations in this paper—based on the OEI case only—already overestimate the reference values in Ref. [17], this was considered sufficient to proceed, following a worst-case approach.

From Section 3.1.2, it was learned that, with the HAPSS aircraft, the TOD increases slightly compared to the reference aircraft, although the MTOM was reduced from 19.5 t to 19.1 t. This increase is caused by the additional drag. Furthermore, with an MTO power setting of 1775 kW–based on the rated MTO power of the reference aircraft–the 2.4% gradient requirement in the second-segment climb could not be achieved. An MTO power of at least 1865 kW would be necessary. Given the worst-case approach (as described above), this value could reduce when more refined models are available. Nevertheless, a shaft power of 1865 kW seems feasible, as a maximum shaft torque of 14,913 Nm and a maximum rotational speed of 1212 rpm could be applied [20], which results in 1893 kW maximum power. This remains to be checked for the exact propeller (sub)type to be applied for the HAPSS aircraft, during the subsequent design phases. For the FCS, the 1865 kW is also not limiting, as this power can be delivered easily when at least three of the four FCS modules are in operation.

It was also found that a gradual increase in power at the first part of the takeoff phase reduces cooling demand drastically (more than 60% during the early takeoff phase), whereas it increases the TOD with 9 to 20%. The second-segment climb gradient is not impacted by this gradual power increase.

The takeoff simulations were restricted to ISA (sea level) conditions, with a dry runway, no ice, no runway slope and no wind, in accordance with Ref. [16]. Nevertheless, the current models can be extended to also simulate the other conditions, as part of future work.

The findings from Section 3.1 are also applicable to the go-around phase. The required MTO power needed for the takeoff phase was found to be sufficient for the OEI case in the go-around (or missed approach) phase, as described in Section 3.2.1.

In Section 3.1.3, it was already acknowledged that several model parameters are still subject to uncertainty. A more refined version of the drag polar could improve the takeoff performance simulations (e.g., taking into account Reynolds number dependencies). Especially, the estimation of the additional parasite drag of the HAPSS aircraft due to the

increased wetted surface of the nacelles and ram air drag of the TMS was based on a rough estimation. Nevertheless, it was learned from the sensitivity analysis in Section 3.1.3 that changes to the parasite drag coefficient C_{D_0} do affect the TOD and climb gradient, but changes to the induced drag coefficient k, and especially the propeller efficiency, have a larger impact. Therefore, further validation and improvements to the modelling of both the propeller and the aerodynamic coefficients are recommended for further work.

From the takeoff simulations, it was learned that an FCS with 3.1 MW-rated power would be sufficient to achieve the takeoff requirements, when taking into account that three out of four FCS modules will be always available, based on the electric architecture with cross-connections between the two HPS nacelles (see Figure 10). If these cross-connections are not feasible, the 1865 kW MTO shaft power needs to be provided by two FCS modules, which would result in a higher total FCS rated power. If the lower-rated FCS of 3.1 MW is applied, it is recommended to reduce the cruise altitude and speed, as is explained in Section 3.2.3. Also, from the climb simulations in Section 3.2.2, it was learned that a 3.1 MW-rated FCS has strong limitations on the climb performance (e.g., a climb time of at least one hour to FL240, making that altitude practically unfeasible). With a 4.2 MW-rated FCS, an improved climb performance could be achieved. However, the 4.2 MW-rated FCS would require a larger volume and mass than the 3.1 MW-rated FCS (estimated mass increase of ~0.7 t, see Table 7), which needs to be compensated for by a lower payload, when taking into account a fixed MTOM (see Table 1). These mass estimations were based on a fixed specific power value [13], which could be improved by more detailed modelling of the FCS component masses.

The volume modelling of the FCS was not part of this work. It is recommended to include this in future work (together with improved FCS component mass estimations). A larger FCS volume could result in a larger parasite drag, in case the nacelles need to be increased. Nevertheless, a higher-rated FCS will operate at a higher efficiency: if the same power as with the lower-rated FCS is applied, this then requires a lower power fraction, which results in an increased FCS efficiency (see also Figure 13). This efficiency increase may compensate for the drag penalty. Furthermore, it reduces the cooling demand, which could result in a smaller TMS (and therefore counteract the increased nacelle size and corresponding drag). An integrated tradeoff of various FCS ratings, taking into account efficiency, mass, drag and, eventually, aircraft performance (e.g., in terms of climb rate, payload, range and energy consumption) still needs to be performed. It is recommended to include this in future work.

It needs to be remarked, though, that the FCS performance simulations were based on simplified modelling. The stack operating pressure was based on a fixed value of 1.6 bar(a), but this could be varied and optimized [35]. The compressor was modelled with fixed efficiencies instead of performance maps. A power limit of the FCS for various altitudes was adopted from Ref. [34], which strongly impacts the climb and cruise performance limits. Optimization of the stack operating pressure and evaluations of other compressor setups (e.g., with additional stages, or multiple compressors) could push this power limit; however, mass penalties (and possibly efficiency penalties) must be taken into account. Such analysis requires enhanced compressor models (e.g., with performance maps and mass estimates) which could be part of future work. In addition, the model of the whole air supply system could be enhanced. For instance, a turbine could be taken into account to support the compressor, which harvests power from the FC stack moist air exhaust.

The simplification of the FCS modelling has limited impact on the takeoff performance, though, as the shaft power requirements were focused on here. Nevertheless, improved models of the FCS will also impact the FCS cooling demand during takeoff. Part of these improvements could also be to model interaction between the TMS sizing and FCS sizing

(during takeoff) and corresponding trade-offs, e.g., the relations between FCS operating temperature, efficiency, mass, heat capacity and TMS sizing. In addition, the estimation of the power needed by the TMS, including the power needed to cool the EPU, could be part of this improvement.

Finally, the model enhancements could also include batteries, e.g., to provide startup power and to reduce the FCS peak power demands, which could also result in a smaller TMS [13] (and therefore smaller nacelles). Table 8 summarizes the modelling limitations and recommendations for future research, discussed above.

Table 8. Summary of modelling limitations and corresponding recommendations for future work.

Modelling Limitation	Recommendation for Future Work
Simplified estimations of drag were applied (literature-based drag polar coefficients of the reference aircraft and drag estimations of the increased nacelle and added cooling ducts).	Apply a more refined drag analysis (e.g., with CFD) of the reference aircraft and of the increased nacelles and cooling ducts (e.g., taking into account the Meredith effect [39]).
Propeller performance was based on a map derived from the literature.	Enhance the propeller modelling, taking into account the specific propeller blades and operating limits that will be used for the HAPSS aircraft.
Exhaust thrust of the reference aircraft engine was not taken into account.	Improve the engine performance model (including exhaust thrust impact).
The takeoff accelerate–stop case was not simulated in this study.	Extend the takeoff simulations with accelerate–stop distance estimation.
Takeoff performance simulations were restricted to ISA (sea level) conditions, with a dry runway, no ice, no runway slope and no wind.	Extend the takeoff simulations to other conditions.
The FCS performance simulations were based on simplified modelling (fixed stack operating pressure, fixed compressor efficiency, power limits).	Extend the analysis with optimization of the FC stack operating pressure and enhanced modelling of the air supply system (evaluating multiple compressor setups and potentially a supporting turbine).
FCS mass estimations were based on a fixed specific power value. FCS volume effects were not taken into account.	Improve FCS mass and volume estimations by more detailed modelling of the FCS components. Perform an integrated tradeoff of various FCS ratings, taking into account efficiency, mass, drag and, eventually, aircraft performance (e.g., in terms of payload, range, climb rate and energy consumption).
The power needed by the TMS is modelled in a simplified way (only the coolant pump power is estimated in relation to the heat load). The power needed to cool the EPU was not taken into account.	Enhance the TMS modelling, including the EPU cooling and the interaction between the TMS sizing and FCS sizing and corresponding tradeoffs.
Batteries were not taken into account in the study.	Assess the use of batteries in future modelling, e.g., to provide startup power and to reduce the FCS peak power demands.

5. Conclusions

Mission performance models have been created for conceptual analysis of the HAPSS modified Dash 8-300. The models were (partially) validated by comparing the reference aircraft predictions against available performance data.

The focus of this paper was on the performance in the takeoff, climb, cruise and go-around phases. From the analyses, it follows that the HAPSS aircraft has a slightly increased TOD as compared to the reference aircraft and that it requires an MTO power of 1865 kW to satisfy the gradient requirement during the second-segment climb, during takeoff and

during the go-around phase. It was also found that a gradual power ramp-up at the first part of the takeoff phase reduces cooling demand drastically (more than 60% during the early takeoff phase), whereas it increases the TOD (up to 20%). The second-segment climb gradient is not impacted by this power ramp-up.

A total rated FCS power of 3.1 MW was found sufficient to satisfy the takeoff and go-around requirements, under the system architecture assumption that, if one propeller fails, the other propeller can receive power from at least three FCS modules. However, with this FCS sized for takeoff, the Dash 8-300 ceiling altitude of 25,000 ft (7620 m) and typical cruise speed of 133 m/s could not be achieved. The operationally optimal cruise point was found to be 5800 m altitude with a cruise speed of 112 m/s. Furthermore, it was found that a higher-rated FCS will be needed to achieve a climb performance that gets closer to the reference aircraft climb profile. A higher-rated FCS may also allow for a lower cooling demand during takeoff, but it comes with mass and volume penalties and potentially drag penalties, which need to be further investigated as part of future work.

Finally, it should be remarked that the findings in this paper are still subject to uncertainty as many model parameters had to be estimated. A sensitivity analysis of these parameters showed that the propeller efficiency has the largest impact on takeoff performance, followed by the induced drag factor and the parasite drag coefficient. Improved parameter estimations, more detailed modelling and further analysis are recommended as part of future work during the subsequent design phases in the HAPSS project.

Author Contributions: Conceptualization, W.L.; Formal analysis, E.S. and P.-J.D.; Funding acquisition, W.L.; Investigation, E.S. and P.-J.D.; Methodology, W.L., P.-J.D. and E.S.; Project administration, W.L.; Software, P.-J.D. and E.S.; Supervision, W.L.; Validation, E.S. and P.-J.D.; Visualization, E.S. and P.-J.D.; Writing—original draft, W.L. and P.-J.D.; Writing—review and editing, W.L., P.-J.D. and E.S. All authors have read and agreed to the published version of the manuscript.

Funding: This research was funded by the Dutch ministry of Infrastructure and Water management in the context of the "Luchtvaart in Transitie" (Aviation in Transition) program, which is part of the National Growth Fund.

Data Availability Statement: Certain data may be obtained from the authors.

Acknowledgments: The authors would like to acknowledge the HAPSS project partners and, in particular, Bidin Suleimanovic and Bartjan Rietdijk (from Conscious Aerospace) for their discussion and input to the performance analyses.

Conflicts of Interest: The authors declare no conflicts of interest. The funders had no role in the design of the study; in the collection, analyses, or interpretation of data; in the writing of the manuscript; or in the decision to publish the results.

References

1. Home | Clean Aviation. Available online: https://www.clean-aviation.eu/ (accessed on 2 November 2024).
2. Homepage—Clean Hydrogen Partnership. Available online: https://www.clean-hydrogen.europa.eu/index_en (accessed on 2 November 2024).
3. Clean Sky 2 Joint Undertaking, Fuel Cells and Hydrogen 2 Joint Undertaking and McKinsey & Company. Hydrogen Powered Aviation: A Fact-Based Study of Hydrogen Technology, Economics, and Climate Impact by 2050, Luxembourg, 22 July 2020. Available online: https://op.europa.eu/en/publication-detail/-/publication/55fe3eb1-cc8a-11ea-adf7-01aa75ed71a1/language-en (accessed on 20 January 2025).
4. Airbus ZEROe. 2024. Available online: https://www.airbus.com/en/innovation/energy-transition/hydrogen/zeroe (accessed on 30 October 2024).
5. Lvovich, V.; Perkins, D.; Lavelle, T.; Hanlon, P.; Hasseeb, H.; McNichols, E.; Holland, F. Commercially-viable Hydrogen Aircraft for Reduction of Greenhouse Emissions. In Proceedings of the 26th International Society for Air Breathing Engines (ISABE) Conference, Toulouse, France, 22–27 September 2024.

6. Ramm, J.; Rahn, A.; Silberhorn, D.; Wicke, K.; Wende, G.; Papantoni, V.; Dahlmann, K. Assessing the Feasibility of Hydrogen-Powered Aircraft: A Comparative Economic and Environmental Analysis. *J. Aircr.* **2024**, *61*, 1337–1353. [CrossRef]
7. Debney, D.; Beddoes, S.; Foster, M.; James, D.; Kay, E.; Kay, O.; Wilson, R. Zero-carbon emission aircraft concepts. In *Aerospace Technology Institute Fly Zero Report FZO-AIN-REP-0007*; Aerospace Technology Institute: Cranfield, UK, 2022.
8. Luchtvaart in Transitie. "Aviation in Transition". Available online: https://luchtvaartintransitie.nl/en (accessed on 2 November 2024).
9. Sahoo, S.; Zhao, X.; Kyprianidis, K. A review of concepts, benefits, and challenges for future electrical propulsion-based aircraft. *Aerospace* **2020**, *7*, 44. [CrossRef]
10. Adler, E.J.; Martins, J.R. Hydrogen-powered aircraft: Fundamental concepts, key technologies, and environmental impacts. *Prog. Aerosp. Sci.* **2023**, *141*, 100922. [CrossRef]
11. Lammen, W.F.; Peerlings, B.; van der Sman, E.S.; Kos, J. Hydrogen-powered propulsion aircraft: Conceptual sizing and fleet level impact analysis. In Proceedings of the 9th European Conference for Aeronautics and Space Sciences (EUCASS), Lille, France, 27 June–1 July 2022.
12. Home—ZeroAvia. Available online: https://zeroavia.com/ (accessed on 30 October 2024).
13. Rietdijk, B.; Selier, M. Architecture design for a commercially viable hydrogen-electric powered retrofitted regional aircraft. In Proceedings of the ICAS Conference, Florence, Italy, 9–13 September 2024.
14. Tiwari, S.; Pekris, M.J.; Doherty, J.J. A review of liquid hydrogen aircraft and propulsion technologies. *Int. J. Hydrogen Energy* **2024**, *57*, 1174–1196. [CrossRef]
15. HAPSS. Available online: https://www.hapss.eu/ (accessed on 30 October 2024).
16. Easy Access Rules for Large Aeroplanes (CS-25)—Revision from January 2023 | EASA (europa.eu). Available online: https://www.easa.europa.eu/en/document-library/easy-access-rules/online-publications/easy-access-rules-large-aeroplanes-cs-25 (accessed on 2 November 2024).
17. Q300 Dash 8 The Quiet One, Airport Planning Manual (APM), PSM 1-83-13, Bombardier Inc. Issue 2, 27 July 2001. Available online: https://dehavillandportal.com/assets/public-documents/D8300-APM.pdf (accessed on 20 January 2025).
18. CemAir/De Havilland-Dash 8 Q300. Available online: https://www.cemair.co.za/fly/general/dehavilland_dash8-q300.php (accessed on 20 January 2025).
19. Type-Certificate Data Sheet No. EASA.IM.A.191 For DHC-8, EASA Issue 16, 3 February 2023. Available online: https://www.easa.europa.eu/sites/default/files/dfu/EASA%20TCDS_DHC-8_Iss%2016%20EASA.IM_.A.191.pdf (accessed on 20 January 2025).
20. Type-Certificate Data Sheet No. IM.E.041 for PW100 Series Engines, EASA Issue: 07, 20 December 2023. Available online: https://www.easa.europa.eu/sites/default/files/dfu/EASA.IM_.E.041_TCDS_Issue_7.pdf (accessed on 20 January 2025).
21. MASS Tool Flyer. Available online: https://www.nlr.org/flyers/en/f543-analyse-the-energy-performance-of-aircraft.pdf (accessed on 2 November 2024).
22. Aircraft Performance Database > DH8C (Eurocontrol.Int). Available online: https://contentzone.eurocontrol.int/aircraftperformance/details.aspx?ICAO=DH8C&NameFilter=dash (accessed on 2 November 2024).
23. BOMBARDIER Dash 8 Q300 | SKYbrary Aviation Safety. Available online: https://skybrary.aero/aircraft/dh8c (accessed on 2 November 2024).
24. Shinkafi, A.; Mohammed, A.; Isah, A. Estimation of Drag Polar for ABT-18 Unmanned Aerial Vehicle. *Niger. Res. J. Eng. Environ. Sci.* **2021**, *6*, 357–365. [CrossRef]
25. Gunnam, R.S. Design of a Regional Hybrid Transport Aircraft. Master's Thesis, San Jose State University, San Jose, CA, USA, May 2019.
26. Quillet, D.; Boulanger, V.; Rancourt, D.; Freer, R.; Bertrand, P. Parallel hybrid-electric powertrain sizing on regional turboprop aircraft with consideration for certification performance requirements. In Proceedings of AIAA Aviation 2021 Forum, Virtual, 28 July 2021; p. 2443. [CrossRef]
27. Roskam, J. *Airplane Design: Preliminary Sizing of Airplanes*; DARcorporation: Lawrence, KS, USA, 1985.
28. Obert, E. *Aerodynamic Design of Transport Aircraft*; IOS Press: Amsterdam, The Netherlands, 2009.
29. BOMBARDIER DASH-8-200-300—SmartCockpit—Airline Training Guides, Aviation, Operations, Safety. Available online: https://www.smartcockpit.com/my-aircraft/bombardier-dash-8-200-300/ (accessed on 2 November 2024).
30. Torenbeek, E. *Synthesis of Subsonic Airplane Design*; Delft University Press: Delft, The Netherlands, 1982.
31. Raymer, D. *Aircraft Design: A Conceptual Approach*; American Institute of Aeronautics and Astronautics, Inc.: Reston, VA, USA, 2012.
32. Suleimanovic, B. (Conscious Aerospace, Ypenburg, The Netherlands). Personal communication, 2024.
33. Janes P&WC PW100. Available online: https://customer.janes.com/display/JAE_0484-JAE_ (accessed on 20 January 2025).
34. Schröter, J. Fuel Cell Air Supply for Hydrogen Electric Propulsion Systems in Aircraft Applications. Ph.D. Thesis, Universität Ulm, Ulm, Germany, 13 June 2023. [CrossRef]

35. Schröder, M.; Becker, F.; Kallo, J.; Gentner, C. Optimal operating conditions of PEM fuel cells in commercial aircraft. *Int. J. Hydrogen Energy* **2021**, *4*, 33218–33240. [CrossRef]
36. Larminie, J.; Dicks, A.; McDonald, M.S. *Fuel Cell Systems Explained*; John & Wiley: Chichester, UK, 2003; Volume 2, pp. 207–225.
37. Van Benthem, R.C. Hydrogen Range Extender for Electric Aircraft—Feasibility Study. In *NLR Contract Report*; NLR-CR-2020-439; NLR: Amsterdam, The Netherlands, December 2020.
38. Turboprop Engine. Available online: https://www.grc.nasa.gov/www/k-12/airplane/Animation/turbtyp/etph.html (accessed on 2 November 2024).
39. Meredith, F.W. *Cooling of Aircraft Engines with Special Reference to Ethylene Glycol Radiators Enclosed in Ducts*; Technical Report; HM Stationery Office: London, UK, 1935.